

# Mapping the physico-chemical properties of mineral dust in Western Africa: Mineralogical composition

P. Formenti<sup>1</sup>, S. Caquineau<sup>2</sup>, K. Desboeufs<sup>1</sup>, A. Klaver<sup>1</sup>, S. Chevaillier<sup>1</sup>, E. Journet<sup>1</sup>, and J. L. Rajot<sup>1,3</sup>

<sup>1</sup> LISA, UMR CNRS 7583, Université Paris Est Créteil et Université Paris Diderot, Institut Pierre Simon Laplace, Créteil, France

<sup>2</sup> IPSL/LOCEAN, UMR 7159 - IRD-CNRS-UPMC-MNHN, Institut de Recherche pour le Développement, Bondy, France

<sup>3</sup> IEES, UMR IRD 242 – IRD – UPMC – CNRS – UPEC - AgroParisTech, Bondy, France

## Abstract

In the last few years, several ground-based and airborne field campaigns have allowed exploring the properties and impacts of mineral dust in Western Africa, one of the major emission and transport areas worldwide. In this paper, we explore the synthesis of these observations to provide with a large-scale quantitative view of the mineralogical composition and its variability with source region and time after transport.

This work reveals that mineral dust in Western Africa is a mixture of clays, quartz, iron and titanium oxides, representing at least 92% of the dust mass. Calcite ranged between 0.3 and 8.4% of the dust mass depending on the origin. Our data do not show a systematic dependence of the dust mineralogical composition with origin, likely as in most of the cases they represent the composition of the atmospheric burden after 1–2 days after emission, when air masses mix and give raise to a more uniform dust load. This has implications for the representation of the mineral dust composition in regional and global circulation models, and satellite retrievals.

Iron oxides account for  $58 \pm 7\%$  of the mass of elemental Fe, and between 2 and 5% of the dust mass. Most of them are composed of goethite, representing between 52 and 78% of the iron oxide mass. We estimate that titanium oxides account for 1-2% of the dust mass, depending on whether the dust is of Saharan or Sahelian origin.

The mineralogical composition is a critical parameter to estimate the radiative and biogeochemical impact of mineral dust. The results on dust composition have been applied to estimate the optical properties as so as the iron fractional solubility of Saharan and Sahelian dust.

36 Data presented in this paper are provided in numerical form upon email request while they  
37 are being implemented as a public database, the Dust-Mapped Archived Properties (DUST-  
38 MAP), an open repository for compositional data from other source regions in Africa and  
39 worldwide.

## 40 **1. Introduction**

41 Mineral dust from wind-driven soil erosion is an important player in the climate system. It is  
42 emitted in large quantities from arid and semi-arid regions of the globe, mostly Africa, Asia,  
43 Australia and North America (Shao et al., 2011), accounting for about 2000 Mt to the annual  
44 aerosol emissions at the global scale. Once in the atmosphere, mineral dust has several  
45 climatic and environmental impacts, related to its ability of scattering and absorbing radiation,  
46 both in the solar and terrestrial spectra, of acting as giant cloud and ice nuclei, of altering the  
47 concentrations of some gaseous pollutants (such as ozone), and of providing nutrients to the  
48 ecosystems via dry and wet deposition, whereby also changing the surface albedo (Shao et  
49 al., 2011; Mahowald et al., 2011). The relevance of those phenomena can be expressed in  
50 terms of radiative forcing, whose magnitude, in terms of central values, is estimated to be as  
51 high as  $0.5\text{--}1\text{ W m}^{-2}$  at the global scale (Mahowald et al., 2011).

52 However, uncertainties remain important, because of the spatial heterogeneity of  
53 concentrations, due to localized emission and short residence time in the atmosphere (1  
54 week at the most, depending on particle size), but also because of the far from satisfactory  
55 knowledge on the underlying physico-chemical properties, composition, size and shape,  
56 ruling the optical, chemical and physical interactions of mineral dust with radiation and the  
57 atmospheric/terrestrial/oceanic constituents (Formenti et al., 2011a).

58 This is particularly the case of the composition. Dust is made of different minerals, whose  
59 proportions, at emission, depend on the mineralogy of the source region and surface wind  
60 speed relative to the soil roughness, which determines their size distribution (Marticorena  
61 and Bergametti, 1995, Alfaro et al. 1998). The various minerals, clays, quartz, potassic and  
62 sodic feldspars, calcium-rich carbonates and sulphates, iron and titanium oxides, have  
63 different mineralogical and crystallographic properties, therefore they may act differently with  
64 respect to light extinction, absorption of water, and surface reactivity (Pye, 1987). For  
65 example, iron oxides have been shown to control the interaction with light in the UV-visible  
66 spectrum (Sokolik and Toon, 1999), whereas quartz, clays and Ca-rich carbonates become  
67 important when looking at the infrared part of the radiation spectrum (Sokolik et al., 1998).  
68 Clays but also feldspars come to play when it comes in investigating the capacity of dust of  
69 activating as ice nuclei at low temperature (Hoose et al., 2008; Atkinson et al., 2013),  
70 whereas calcite (calcium carbonate) shows high surface reactivity with respect to various  
71 atmospheric pollutants (Crowley et al., 2010). Another clay family, the smectites, bears the

72 most soluble iron which might become available as nutrient to the marine phytoplankton  
73 (Journet et al., 2008). The properties of mineral dust are size-dependent, and the  
74 dimensional spectrum of mineral dust particles at emission extends over various orders of  
75 magnitude from approximately 200-300 nm to 100  $\mu\text{m}$  (Kandler et al., 2009) depending on  
76 wind speed at emission. As a consequence, the properties of mineral dust vary as a function  
77 of time after emission due to size-dependent deposition, mixing, and gaseous condensation.  
78 Because these processes are not well established, the physico-chemical properties of  
79 mineral dust have to be determined experimentally at the various times of their life cycle.

80 In this paper, we relate on the mineralogical and chemical composition of mineral dust from  
81 Western Africa at emission or at most within 1–2 days from emission. The southern Sahara  
82 is the location of two of most persistent dust sources at the global scale, the Bodélé  
83 depression in between the Tibesti and the Ennedi mountain chains in Chad, and the areas in  
84 between the east of Mauritania, the North of Mali and the south of Algeria (Prospero et al.,  
85 2002; Laurent et al., 2008; Washington et al., 2006; Shao et al., 2011). These sources are  
86 relevant at the global scale as their emissions are transported across the Atlantic Ocean  
87 towards South and Central America (Reid et al., 2003; Koren et al., 2006; Ben-Ami et al.,  
88 2009; 2010).

89 The atmospheric content of mineral dust in Western Africa shows a very pronounced  
90 seasonal cycle despite high variability, both at the daily and inter-annual scales (N'Tchayi et  
91 al., 1994; N'Tchayi Mbourou et al., 1997; Goudie and Middleton, 2001). This is largely  
92 explained by the alternance of two meteorological regimes. Throughout the year, the  
93 “Harmattan”, a north-eastern dry wind, is responsible for intense dust emissions in the arid  
94 areas of the Sahara and very efficient transport towards the Atlantic Ocean and across the  
95 Sahel (Pye, 1987; Sokolik et al., 2001; Laurent et al., 2008). Wintertime is also the biomass  
96 burning season south of approximately 13°N (Haywood et al., 2008), and mixing between  
97 dust and biomass burning aerosols might occur during southward transport (Johnson et al.,  
98 2008). During summer, the Inter Tropical Convergence Zone (ITCZ) displaces northward,  
99 allowing the surface Monsoon flow to intrude the continent from the South-West towards the  
100 continental Sahel. This shift induces a progressive organization of convection from isolated  
101 cells to large-scale fast propagating systems, which, particularly at the beginning of the  
102 Monsoon season, are often not precipitating, and efficient in eroding bare soils and  
103 producing mineral dust (Marticorena et al., 2010; Abdourhamane Touré et al., 2011). The  
104 summertime column dust content over western Africa results therefore from the  
105 superimposition of local emission from the Sahel and remote transport of dust emitted in the  
106 Sahara (Tegen and Fung, 1994; Yoshioka et al., 2005; Marticorena et al., 2010).

107 The mineralogy of the Saharan and Sahelian source areas have different mineralogy: the  
108 Sahara is mainly composed by calcisols or arenosols, whereas the Sahel is richer in  
109 weathered plinthosols (Fe oxides/kaolinite/quartz) (Pye, 1987; Claquin et al., 1999;  
110 Caquineau et al., 2002; Nickovic et al., 2012; Journet et al., 2014). As a consequence,  
111 mixing or layering of dust transported from the Sahara and locally emitted by convection over  
112 the Sahel should be detectable through differences in the composition over the atmospheric  
113 column.

114 Furthermore, western Africa is prone to land-use change because of the rapid demographic  
115 increase and desertification during drought periods (ECA, 2005; Dai, 2011), which could  
116 feedback in increased emission (Carslaw et al., 2010). Rajot (2001) have shown that, in the  
117 Sahel, additional emission by wind erosion of mesoscale meteorological disturbances, such  
118 as organized convective systems, occurs on harvested soils only. These additional  
119 emissions, anthropogenic in origin, are not quantified to date (Boucher et al., 2013).

120 To provide with the quantitative estimate of the mineralogical composition of mineral dust at  
121 the regional scale, we report in this paper the synthesis of data from various aircraft and  
122 ground-based field campaigns which have taken place in western Africa in 2006 and 2007.  
123 These are the African Monsoon Multidisciplinary Analysis (AMMA) Special Observing Period-  
124 0 (SOP0; Rajot et al., 2008), augmented of the airborne Dust and Biomass-burning  
125 Experiment (DABEX; Haywood et al., 2008), and Special Observing Period-1 and -2 (SOP1-  
126 2; Reeves et al., 2010); the Dust Outflow and Deposition to the Ocean (DODO; McConnell et  
127 al., 2008) and the Geostationary Earth Radiation Budget Intercomparison of Longwave and  
128 Shortwave radiation (GERBILS; Haywood et al., 2011).

129 Some of the data discussed in this paper have been published previously (Formenti et al.,  
130 2008; 2011b; Rajot et al., 2008; Klaver et al., 2011). Here, they are revisited with a broader  
131 perspective discussion of the mineralogical variability at the regional scale of Western Africa  
132 and its implications for climate.

133 This paper discusses whether, when mapped at the scale of western Africa, the regional  
134 variability at emission deriving from the heterogeneity of the mineralogy of the parent soils is  
135 still relevant or whether it becomes irrelevant when dust is airborne. This is important for  
136 developing a model parameterisation for dust in regional and global climate models or for  
137 satellite retrieval algorithms.

## 138 **2. Methods**

139 Full details of the field campaigns operations, experimental procedures, collection and  
140 analytical protocols are described in a number of companion papers (Hawwood et al., 2008;

141 2011; Formenti et al., 2008; 2011b; Rajot et al., 2008; McConnell et al., 2008; 2010; Klaver et  
142 al., 2011) which are resumed hereafter.

## 143 **2.1. Field campaigns**

144 The African Monsoon Multidisciplinary Analysis (AMMA) was an international project to  
145 improve our knowledge and understanding of the West African monsoon (WAM), its  
146 variability on daily-to-interannual time scales, and its effects on the status of the atmosphere  
147 (Redelsperger et al., 2006). Because of its links to precipitation, wind speed, soil surface  
148 state, and drought at different time scales, mineral dust aerosols play a role in this  
149 comprehensive scientific framework.

150 The experimental strategy of the AMMA program was based on embedded multi-year,  
151 seasonal and intensive observation periods (Janicot et al., 2008; Lebel et al., 2010). The  
152 observations used in this paper were conducted during the intensive observations periods,  
153 called Special Observing Periods (SOPs). The wintertime SOP (SOP0), was dedicated to the  
154 investigation of mineral dust and biomass burning, and their mixing, took place from 13  
155 January and 13 February 2006. The summertime observations (periods SOP1 and SOP2)  
156 started on 31 May 2006 and ended on 17 July 2006 and were dedicated to the fine  
157 description of the interactions between aerosols and convection.

158 The ground-based observations were conducted at the AMMA supersite of Banizoumbou  
159 (13.5°N; 2.6°E, 250 m above sea level), located at a remote location at about 60 km east  
160 from the capital of Niger, Niamey. This site has been operational since the early 1990s, when  
161 the first measurements of soil erosion were performed on a cultivated field and a fallow  
162 (Rajot, 2001). Since 1995, the site is also an Aerosol Robotic Network (AERONET) station  
163 measuring columnar aerosol optical properties. The ground-based site operations are fully  
164 described in Rajot et al. (2008).

165 The aircraft observations were conducted from Niamey, Niger. The wintertime airborne  
166 campaign, called AMMA SOP0-DABEX, was conducted onboard the Facility for Airborne  
167 Atmospheric Measurements (FAAM) BAe-146 aircraft (Haywood et al., 2008). The aircraft  
168 performed thirteen research flights in the area between 8°N and 18°N, including three  
169 dedicated excursion to the north of Niger, toward the Air Mountains and the Ténéré desert to  
170 probe specifically mineral dust whilst transport. In summertime, the observations were  
171 conducted onboard the Service des Avions Français Instruments pour la Recherche en  
172 Environnement (SAFIRE) ATR-42, which operated twenty research flights in the area  
173 between 6° and 20°N, therefore crossing the ITCZ to the north to contrast the Sahara and  
174 the Sahelian dust properties in their respective boundary layers (Reeves et al., 2010;  
175 Formenti et al., 2011b).

176 The Geostationary Earth Radiation Budget Intercomparison of Longwave and Shortwave  
177 radiation (GERBILS) found its scientific motivation in the discrepancy that had been found  
178 between the satellite observations and the numerical weather model predictions of the top of  
179 the atmosphere outgoing longwave radiation over desert areas in western Africa (Haywood  
180 et al., 2005). This discrepancy could be reconciled by including mineral dust in the model.  
181 The GERBILS experiment, whose full rationale and operating details are described in  
182 Haywood et al. (2011), was therefore designed to test this hypothesis, and to determine the  
183 properties of the mineral dust to be included in the model. The experiment consisted in ten  
184 research flights onboard the FAAM BAe-146 performed between Nouakchott (18.10°N,  
185 15.94°W, Mauritania) and Niamey (13.48°N, 2.18°E, Niger) on an almost standard route  
186 along the 18°N meridian. Flights were performed between 18 and 29 June 2007, in a period  
187 characterised by a persistent and widespread dust load.

188 Finally, the Dust Outflow and Deposition to the Ocean (DODO) airborne experiment took  
189 place at two different periods in 2006: in wintertime (7–16 February) and in summertime (22–  
190 28 August). The aim of DODO was to characterised dust as a possible nutrient for the marine  
191 ecosystems. For this reason, the FAAM BAe-146 aircraft was based in Dakar, in Senegal,  
192 and most of the twelve research flights (six in the winter period and six in the summer period,  
193 respectively) were conducted over the Atlantic Ocean in the outflow from the African  
194 continent. However, two flights, one per season, were performed inland above Mauritania in  
195 order to sample dust at or very close after emission (McConnell et al., 2008).

## 196 **2.2. Sample collection and handling**

### 197 **2.2.1. Ground-based**

198 Aerosol sampling at the ground-based AMMA super site of Banizoumbou was performed  
199 using two identical purpose-built wind-oriented inlets designed for the AMMA field campaigns  
200 (Rajot et al., 2008). The cut-off diameter 50% efficiency of these inlets has been calculated to  
201 be approximately 40  $\mu\text{m}$  by using the standard formulae of particle losses in inlets and  
202 tubings reported in Baron and Willeke (2001) and Hinds (1999). Each inlet leads to a  
203 sampling chamber containing seven different sampling lines, each of them dedicated to a  
204 different instrument. Multiple sampling lines are very convenient as they allow collecting  
205 various filter samples in parallel, differentiated and optimized in terms of sampling medium,  
206 exposure interval and flow rate as a function of the analytical technique to be applied. This  
207 also results in minimal manipulation of the filters after sampling. Samples were collected on  
208 acid washed 42-mm polycarbonate Nuclepore filters (0.4  $\mu\text{m}$  pore size) mounted on plastic  
209 rings. Samples were stored in Petri dishes after sampling. Sampling time was of the order of  
210 hours, and was varied depending on the aerosol mass concentration measured on-line by a

211 Tapered Element Oscillating Microbalance (TEOM, Rupprecht and Patashnick, Albany, USA)  
212 (Rajot et al., 2008).

### 213 **2.2.2. Airborne**

214 During the AMMA SOP0-DABEX, DODO and GERBILS campaigns, samples were collected  
215 onboard the FAAM BAe-146 aircraft. The aircraft is capable of carrying 2 crew, 18 scientists  
216 and a total scientific payload of up to 4000 kg for a distance of 3700 km with a ceiling of  
217 35,000 feet and has a typical science speed of 110 m s<sup>-1</sup>. For the typical scientific payload,  
218 flight patterns, ambient meteorological conditions and the proximity of diversion airports  
219 encountered during the campaigns, the average endurance of the BAe146 aircraft was  
220 approximately 5 hours. Sampling was been performed using a set of two parallel thin-walled  
221 inlet nozzles with a curved leading edge; the design was based on criteria for aircraft engine  
222 intakes at low Mach numbers (Andreae et al., 1988). The sampling system was operated at  
223 flow rates that averaged at 120 L min<sup>-1</sup> (at ambient pressure and temperature; the flow was  
224 adjusted to maintain slightly subisokinetic sampling conditions. The passing efficiency of the  
225 inlets has not been formally quantified. During AMMA SOP-0/DABEX, Chou et al. (2008)  
226 showed that the number size distributions of the aerosols collected on the filters (counted by  
227 electron microscopy) extended up to 10 µm diameters and were of comparable magnitude to  
228 those measured by wing-mounted optical counters.

229 Aerosol particles were sampled by filtration onto two stacked-filter units (SFUs) mounted in  
230 parallel. Each SFU can hold a maximum of three filters on sequential 47- or 90-mm diameter  
231 polyethylene supports. Only one stage was used during the campaigns, i.e., samples  
232 represented the aerosol bulk composition. Samples were collected only during horizontal  
233 flight legs lasting not less than 20 min in order to guarantee sufficient loading of the filter  
234 samples. As a consequence, at the aircraft cruise speed, each sample had at best a spatial  
235 resolution of 180 km. Each SFU consisted of a Nuclepore filter (Whatman) of nominal pore  
236 size 0.4 µm.

237 During the AMMA SOP1-2 campaigns, samples have been collected onboard the SAFIRE  
238 ATR-42. With the necessary payload for the campaign, the aircraft had a maximum  
239 endurance of 4 h. Minimum flight altitude is 300 m over land. Ceiling is approximately 7 km.  
240 The aircraft was equipped with basic sensors for measuring the radiative, dynamic and  
241 thermodynamic properties of the atmosphere (Saïd et al., 2010).

242 Aerosol sampling was performed using the AVIRAD aerosol sampling system newly  
243 developed for AMMA (Formenti et al., 2011b). It consists of an iso-axial and isokinetic inlet  
244 whose 50% passing efficiency has been estimated at 9 µm in diameter. At the cruise speed  
245 of the ATR-42 (93 m s<sup>-1</sup>) the delivered volumetric flow rate is 350 L min<sup>-1</sup>, which was

246 distributed to various instruments, including two SFU for collecting bulk aerosol samples.  
247 Samples were obtained by parallel filtration onto 42-mm diameter polycarbonate membranes  
248 (nominal pore size 0.4  $\mu\text{m}$  Nucleopore, Whatman) on polyethylene supports. Samples were  
249 collected only during horizontal flight legs lasting not less than 20 minutes. Immediately after  
250 each flight, the loaded filters were stored in Petri dishes.

251 Ground-based operation with multiple sampling lines allowed for parallel sampling where the  
252 sampling duration is adapted to the characteristics (detection limit, saturation level) of the  
253 technique to be employed for analysis. On aircraft, the two parallel samples available had to  
254 be manipulated further to allow accommodating the number of analysis one wanted to  
255 perform, also taking into account the fact that some analyses are destructive of the sample.  
256 Therefore, the handling protocol for aircraft samples consisted in analysing entire filters or  
257 portions of those depending on their load on mineral dust. A dedicated tool in polyethylene  
258 has been developed for cutting the 47- or 90-mm filters into halves, quarters or eighth without  
259 touching and therefore contaminating them.

## 260 **2.3. Sample analysis**

### 261 **2.3.1. Elemental composition**

262 The total elemental concentrations for elements from Na to Pb by wavelength dispersive X-  
263 ray fluorescence (WD-XRF) for samples collected on the ground and on the ATR-42 and  
264 Particle-Induced X-ray Emission (PIXE) for the aircraft samples collected onboard the BAe-  
265 146. The reason for using different techniques for ground-based and aircraft samples lays on  
266 the fact that the WD-XRF sample holder set up could not, at the time, host filters which are  
267 not supported on polyethylene frames. The details of the analytical protocols are provided in  
268 Formenti et al. (2008; 2011b), McConnell et al. (2008), Rajot et al. (2008) and Klaver et al.  
269 (2011). Elemental concentrations are estimated with a 5% error. An inter-comparison  
270 exercise on samples generated in the laboratory from geo-standards of known and certified  
271 composition has shown that the two techniques yield comparable results within the error bars  
272 (Formenti et al., 2010).

### 273 **2.3.2. Mineralogical composition**

274 The identification of major minerals composing mineral dust: quartz ( $\text{SiO}_2$ ), calcite ( $\text{CaCO}_3$ ),  
275 dolomite ( $\text{CaMg}(\text{CO}_3)_2$ ), gypsum ( $\text{CaSO}_4 \cdot 2\text{H}_2\text{O}$ ), clays (kaolinite, illite, smectite, chlorite),  
276 feldspars (ortoclase  $\text{KAlSi}_3\text{O}_8$  and albite  $\text{NaAlSi}_3\text{O}_8$ ) was performed by X-ray diffraction  
277 (XRD) analysis at the Institut de Recherche pour le Développement (IRD) in Bondy, France.  
278 The diffractometer, a Siemens D500 with Ni-filtered  $\text{Cu-K}\alpha$  radiation, was operated at 40 kV  
279 and 30mA. Samples were scanned from 2 to 70° ( $2\theta$ ) with counting for 10 s every 0.02° ( $2\theta$ ).  
280 The analytical procedure and semi-quantitative treatment are fully described by Caquineau et



281 al. (1997), who adapted the sample preparation to low-mass mineral aerosol (load deposited  
282 on filter > 800 µg). The calibration protocol that was applied to the XRD spectrometer in  
283 order to quantify the mineralogical composition is described in Klaver et al. (2011). An  
284 improvement of the calibration curves was performed after publication of the Klaver et al.  
285 (2011) paper by achieving the calibration for the feldspars (ortoclase and albite). The  
286 calibration factors  $K_i$  representing the ratio between the peak surface area  $S_i$  in the diffraction  
287 spectra and the mass  $m_i$  of the  $i$ -mineral are reported in Table 1. The error on the mineral  
288 masses is estimated as the sum of the relative error on the peak area in the diffractograms  
289 and on the calibration factor  $K_i$  as  $\frac{\Delta m_i}{m_i} = \frac{\Delta K_i}{K_i} + \frac{\Delta S_i}{S_i}$ . The term  $\Delta K_i/K_i$  is estimated from the  
290 error of the slope of the calibration curve (Table 1) and it varies between 2% and 10%. The  
291 term  $\Delta S_i/S_i$  depends on the abundance of the mineral in the samples and has been estimated  
292 from the obtained counting statistics.

### 293 **2.3.3. Iron oxide content and speciation**

294 The iron oxide content, defined as the fraction of iron which is not in the crystal lattice of  
295 silicates (Karickhoff and Bailey, 1973), was determined with the adapted Citrate-Bicarbonate-  
296 Dithionite (CBD) extraction method developed by Lafon et al. (2004). This method is an  
297 adaptation for aerosol filters (with typical material mass less than 500 µg) of the classical  
298 method of (Mehra and Jackson, 1960) for soil analysis. The method uses a reagent to  
299 dissolve iron oxides selectively via reduction. Details of this analysis are given in Formenti et  
300 al. (2008; 2011b) and Klaver et al. (2011). The percent error on the iron oxide content is  
301 estimated to be 10% as its assessment is based on two XRF analysis (prior and after  
302 dissolution of the iron oxides from the sample).

303 The speciation of iron oxides was performed by X-ray absorption (XAS) at the Fe K-range:  
304 XANES (X-ray Absorption Near Edge Structure) and EXAFS (Extended X-ray Absorption  
305 Fine Structure) at the SAMBA (Spectroscopies Applied to Materials based on Absorption,  
306 <http://www.synchrotron-soleil.fr/portal/page/portal/Recherche/LignesLumiere/SAMBA>) line  
307 SOLEIL synchrotron facility in Saclay, France. XAS spectroscopy is based on the analysis of  
308 the position and shape of the K-pre-edge and edge peaks, depending on the oxidation state  
309 of iron but also to the atomic position of the neighbouring atoms, mostly O<sup>+</sup> and OH<sup>-</sup>. The  
310 quantification of the Fe-status was based on the analysis of five standards of Fe(III)-bearing  
311 minerals which can be found in mineral dust. Full details of the experimental protocols and  
312 the data analysis are provided in *Formenti et al., Dominance of goethite over hematite in iron  
313 oxides of mineral dust from Western Africa: quantitative partitioning by X-ray Absorption  
314 Spectroscopy, submitted to J. Geophys. Res., 2014* (hereafter referred as Formenti et al.,  
315 2014).

## 316 2.4. Data interpretation and presentation

### 317 2.4.1. Source identification

318 The identification of source regions has been performed using a variety of ancillary products:

319 (1) The record of measurements of the horizontal movement of sand grains by a  
320 saltiphone (Eijkelkamp, Giesbeek, The Netherlands) located at the proximity of the sampling  
321 inlets at the super-site of Banizoumbou providing with the estimate of the saltation horizontal  
322 flux related to established local erosion (Sow et al., 2009).

323 (2) Various satellite products, in particular, the daily images of the UV aerosol index by  
324 the Ozone Monitoring Instrument (OMI) on Aura; the instantaneous dust product maps from  
325 the SEVIRI satellite; and the Infrared Difference Dust Index (IDDI) obtained from the infrared  
326 channel of Meteosat (10.5-12.5  $\mu\text{m}$ ) (Legrand et al., 1994).

327 (3) Back-trajectories and air mass dispersion calculations using the Met Office Numerical  
328 Atmospheric-dispersion Modeling Environment (NAME, Cullen, 1993) and the NOAA HYbrid  
329 Single-Particle Lagrangian Integrated Trajectory Model (HYSPLIT) as described in Chou et  
330 al. (2008), Rajot et al. (2008) and Klaver et al. (2011).

### 331 2.4.2. Data presentation

#### 332 2.4.2.1. Calculation of the total mass

333 In the following, the composition of mineral dust will be presented as percent of the total dust  
334 mass (TDM). According to Pye (1987), the TDM can be decomposed as

335

$$336 \quad TDM = m_{clays} + m_{quartz} + m_{Ca-rich} + m_{feldspars} + m_{iron\ oxides} + m_{tit\ oxides} + m_{organic} \quad (1)$$

337

338 where

339  $m_{clays}$  = mass of the major clay-species (kaolinite, illite, smectite, chlorite)

340  $m_{quartz}$  = mass due to quartz ( $\text{SiO}_2$ )

341  $m_{Ca-rich} = m_{calc} + m_{dolom} + m_{gypsum}$  = mass due to calcium carbonates and sulphates in the form  
342 of calcite ( $\text{CaCO}_3$ ), dolomite ( $\text{CaMg}(\text{CO}_3)_2$ ) and gypsum ( $\text{CaSO}_4$ )

343  $m_{feldspars}$  = mass due to feldspars, such as albite and ortoclase ( $\text{NaAlSi}_3\text{O}_8$  and  $\text{KAlSi}_3\text{O}_8$ ,  
344 respectively)

345  $m_{iron\ oxides}$  = mass due to hematite ( $\alpha\text{-Fe}_2\text{O}_3$ ) and goethite ( $\alpha\text{-FeOOH}$ )

346  $m_{tit\ oxides}$  = mass due to titanium oxides ( $\text{TiO}_2$ )

347  $m_{organic}$  = mass due to organic matter which is present in the soils as biological debris and  
348 complex organic molecules (humus).

349

350 In practical terms, the TDM can be approximated by the TEDM (total estimated dust mass)  
351 as the sum of the oxide-equivalent of the elemental concentrations of the major elements in  
352 mineral dust (Al, Si, Fe, Ca, K, Ti accounted as  $Al_2O_3$ ,  $SiO_2$ ,  $Fe_2O_3$ ,  $CaCO_3$ ,  $K_2O$  and  $Ti_2O$ )  
353 whose masses are measured by XRF analysis. The TEDM estimated this way can be  
354 compared to the direct measurement of the total dry gravimetric mass (TDGM), which is  
355 available for some of the datasets (ground-based AMMA SOP0 and SOP1-2, and GERBILS),  
356 either by weighing or by on-line Tapering Element Oscillating Microbalance (TEOM, model  
357 1400a, Rupprecht and Patashnick Albany, New York USA) (see Rajot et al. (2008) and  
358 Klaver et al. (2011)).

359 The slope of the least-squared linear regression between the TEDM and TDGM, calculated  
360 on the 81 samples on which the extraction of iron oxides was performed (see section 3.3), is  
361 0.98 and the coefficient of determination ( $R^2$ ) is 0.88. This is very satisfactory, taking into  
362 account that, because the mass is dominated by coarse particles, which have large mass but  
363 little number, differences might arise by losses of some coarse particles between the time at  
364 which the filter was weighed and the time at which it was analysed by XRF or by small  
365 differences between the filter sampling duration and the TEOM integration times. As a matter  
366 of fact, the most of the scatter in the data is observed for samples which corresponded to  
367 local erosion or transported emission by convective systems, having the largest fraction of  
368 coarse particles and the shortest integration times. This becomes apparent when plotting  
369 separately the ground-based AMMA SOP0 and SOP1-2 data (Figure 1).

370 Therefore, we consider that the TDM is equal to the TDGM for samples for which the TDGM  
371 is measured. When this is not available, the TDM is approximated via the TEDM calculated  
372 as sum of oxides. The percent uncertainty is calculated as the squared sum of the errors on  
373 the calculation of the TEDM from the measured Al, Si, Fe, Ca, K, and Ti elemental masses.  
374 By doing so, the percent uncertainty on the TDM is 12%.

#### 375 **2.4.2.2. Calculation of the mineralogical composition**

376 The mass apportionment presented in Equation 1 has been performed as follows:

- 377 (1) the masses of quartz, calcite, dolomite, gypsum and feldspar ( $m_{quartz}$ ,  $m_{Ca-rich}$ ,  $m_{feldspars}$ )  
378 are quantified by XRD using the mass/intensity calibration curves as described in  
379 section 2.3.

380 (2) The mass of iron oxides ( $m_{iron\ oxides}$ ) is measured directly by CBD analysis. The  
381 apportionment of  $m_{iron\ oxides}$  into its main components (hematite and goethite) is  
382 performed by XANES spectroscopy.

383 (3) the mass of the clay species, kaolinite, illite, smectite, chlorite ( $m_{clays}$ ) is estimated by  
384 the difference between the TDM and sum of the masses of  $m_{quartz}$ ,  $m_{Ca-rich}$ ,  $m_{feldspars}$   
385 and  $m_{iron\ oxides}$ . The apportionment of  $m_{clays}$  into its constituting species is difficult to  
386 achieve without a direct calibration. This is highly uncertain as there is basically no  
387 mineralogical reference having the same crystallographic and chemical status than in  
388 the actual aerosol samples, because of the exposure to the environment, weathering  
389 in particular, that they experience before and after become airborne. Furthermore,  
390 smectite clays are actually a family of species with different chemical characteristics  
391 (see the general chemical formulae in Appendix 1 for montmorillonite and nontronite).  
392 When only illite and kaolinite are present in the samples, and no traces of chlorite or  
393 smectite are shown by XRD analysis, their mass can be apportioned readily using the  
394 illite-to-kaolinite ratios (I/K) established by Caquineau et al. (2002) as a function of  
395 dust source region as

396

$$m_{kaolinite} = \frac{m_{clays}}{1 + \frac{I}{K}} \quad (2)$$
$$m_{illite} = m_{clays} - m_{kaolinite}$$

398

399 When smectites or chlorite is also detected, Equation (2) does not hold true. We will  
400 evaluate in the following sections the uncertainties induced by this approximation.

401 (4) The mass of titanium oxides  $m_{tit\ oxides}$  is estimated by calculating the  $TiO_2$  contribution  
402 as the measured elemental Ti multiplied by 1.67, the ratio between the atomic weight  
403 of  $TiO_2$  and that of elemental Ti;

404 (5) The mass of organic compounds ( $m_{organic}$ ) in mineral dust was generally neglected on  
405 the basis of the work by Lepple and Brine (1976), it should not exceed 3% of the  
406 TDM.

407 (6) We also did not take into account the mass of diatomite fragments which have been  
408 observed in samples originated from Bodélé (Chou et al., 2008). Diatomite fragments  
409 are silicate skeletons of algae and they do not have a crystalline structure which can  
410 be quantified by XRD analysis. Their presence can be put into evidence by elemental  
411 analysis as excessive values of the Si-to-Al ratio, up to 4 (Formenti et al., 2011b). The

412 diatomite mass can therefore be estimated by comparing the excess-SiO<sub>2</sub> mass  
413 calculated from elemental Si concentrations with respect to the mean ratio-to-Al to the  
414 mass of quartz estimated by XRD analysis. When doing so, the excess-SiO<sub>2</sub> mass is  
415 comparable to that of quartz except for the few samples for which dust originated  
416 from the Bodélé depression in which case their contribution to the TDGM is in the  
417 range 6–13%. This contribution is accounted in the error bars of the clay fraction for  
418 these samples.

### 419 **3. Results**

420 The whole dataset (ground-based and airborne AMMA SOP0 and AMMA SOP1-2, GERBILS  
421 and DODO campaigns) consists in 704 samples for which we measured the total elemental  
422 composition. Out of those, 54 samples have been selected to yield data on the major mineral  
423 composition, 86 have been analyzed to yield the content of iron oxide, 12 to determine the  
424 iron oxide speciation. 31 samples combined sufficient information to determine the full  
425 mineralogical composition. The sample selection has been based on the filter loading and on  
426 the possibility of identifying their provenance and attributing them a source region.

#### 427 **3.1. Identification of source regions**

428 The identification of the origin of the mineral dust collected on the samples implies being able  
429 to make the link between the knowledge on the position and the mineralogy of the source  
430 regions to that of the aerosol samples. To do so, one should know (1) the transfer function, at  
431 emission, linking the soil mineralogical/chemical composition to that of the aerosols, and (2)  
432 the transfer function describing how its composition is modified during transport.

433 The first transfer function describes the mineralogical fractionation that occurs between the  
434 soil and the aerosol as a consequence of the size segregation happening when the soil  
435 grains blast on the soil after saltation (Rahn, 1976). The fractionation can alter the elemental  
436 ratio between Si and Al, as a result of the depletion in quartz and feldspars with respect to  
437 clays at emission. Quartz and feldspars have higher Si content than clays and are more  
438 abundant in the sand than in the silt/clay fractions of the soil (Mason, 1966; Rahn, 1976;  
439 Chatenet et al., 1996). These last are enhanced during emission by the  
440 saltation/sandblasting (Alfaro et al., 1998). Whereas there is still no systematic assessment  
441 of the transfer function between the soil and the aerosol composition, Claquin et al. (1999)  
442 have shown that some mass ratios between minerals (for examples, that of illite to kaolinite  
443 and that of calcite to quartz) are conserved from the soil to the aerosol if the comparison is  
444 restricted to roughly the same size fractions (clays or silt). Lafon et al. (2006) also suggested  
445 that the free-iron fraction to the total is conserved. Jeong (2008) has shown that the calcite  
446 and the K-feldspar fractions are very similar in Asian dust and the corresponding silty soil

447 fraction. The percent of phyllosilicate is higher in the dust aerosols than in the soil, whereas  
448 the quartz and plagioclase fractions are lower.

449 The second transfer function describes how the dust composition is modified during  
450 transport. Our dataset consists in data which have been collected at most 2 days after  
451 emission. We expect that only losses of particles of diameter larger than 10  $\mu\text{m}$  would occur  
452 in this short time scale (Pye, 1987). We therefore assume that the chemical/mineralogical  
453 composition of our dust aerosol samples is linkable to that of the parent source regions.

454 To identify the pathway of air masses during transport, and trace them back to an active dust  
455 source, we used back-trajectory and dispersion modelling and various satellite products  
456 (e.g., Chou et al., 2008; Klaver et al., 2011). This approach does not apply to samples  
457 collected in the boundary layer during the Monsoon season south of the Inter-Tropical  
458 Convergence Zone (ITCZ). In this case, the dominant flow is from the south-west: dust is  
459 present in the boundary layer only as a result of erosion by organized convection or under  
460 particularly stable conditions, when high temperatures establish and the thermal turbulence  
461 in the boundary layer raises its top height at or above the shear level, bringing dust from the  
462 free troposphere in the surface level (Flamant et al., 2009; Formenti et al., 2011b).

463 Even when applicable, this approach has various caveats: first, if their horizontal velocity is  
464 high and exceed the local threshold velocity, air masses within the boundary layer might get  
465 loaded with dust along their way before reaching the sampling point. This happens for  
466 example when emission is induced by large scale frontal systems as the one of 3–7 March  
467 2006 (Tulet et al., 2008). Secondly, ground-based sampling lasts several hours and the  
468 direction of air masses might change in between. Finally, aircraft samples integrate over  
469 large areas to which different air masses from different source regions might contribute. This  
470 problem might be overcome, or at least minimized, by increasing as much as possible the  
471 sampling frequency to match the variability of transport. We did that by following the  
472 variability of concentrations, in time or space, with ancillary measurements at higher temporal  
473 resolution (mass concentration by the TEOM balance, or the scattering coefficient by a TSI  
474 nephelometer).

475 In spite of this, we cannot exclude that our samples might represent larger emission areas  
476 than single "hot spots" (see for example, Figure 1 in Klaver et al. (2011)). We do not  
477 necessary regard this as a problem, as the atmospheric dust load, both at short and large-  
478 scale transport, is often due to a variety of sources active at the same time (Glaccum and  
479 Prospero, 1980; Reid et al., 2003; Formenti et al., 2003; Schepanski et al., 2007; Laurent et  
480 al., 2008; McConnell et al., 2008; Marticorena et al., 2010). Also, this supra-imposition, both  
481 in the vertical and in the horizontal, is what is actually seen by spaceborne sensors. The

482 results of this paper might then be used to build a dust composition model on a scale  
483 relevant to satellites.

484 When doing so, we found that samples presented in this paper are representative of major  
485 African sources which, according to Formenti et al. (2011) and Scheuven et al. (2013), are  
486 indicated as PSA (Potential Source Area) in Figure 2.

- 487 • The PSA2, including arid areas in Western Sahara, Mauritania and Morocco,  
488 sampled during the DODO and the GERBILS campaigns. With respect to the extent  
489 of this source, the northern part is under-represented as it was sampled on one  
490 occasion only;
- 491 • The PSA3 represents emitting area in northern Mali and southern Algeria. This is  
492 largely the dominant source in terms of frequency of sampling. The air masses  
493 travelling from PSA3 often show a recirculating pathway over North Niger. By doing  
494 so, at times they might pick up dust from the desert areas close to the Aïr massif,  
495 which is not depicted in Figure 2, before reaching the sampling site. These  
496 occurrences, when identified, are labelled as PSA3-NN;
- 497 • The PSA4 was sampled on a few occasions during wintertime. The PSA4 was  
498 sampled on a few occasions during wintertime. As for PSA3, samples originating from  
499 PSA4 for which the air masses had got in contact with the surface in northern Niger  
500 when satellite images indicated emissions, have been labelled as PSA4-NN;
- 501 • A few samples also represent dust originated from the Bodélé depression (PSA5). In  
502 summertime, a mixture of Sudan and Chad sources including Bodélé might have  
503 been sampled (Flamant et al., 2009). Finally, a number of episodes of erosive  
504 emissions by convection in the Sahel were also sampled and characterised  
505 (referenced as Sahel). These occurred both over Mali and over Niger.

506 The PSA1 source is not represented in this paper as it was not sampled during the field  
507 campaigns.

508

509 To provide with a first link between geographical origin and chemical composition, we traced  
510 the scatterplot of elemental Si/Al versus Fe/Ca which we color-coded according to the source  
511 region according to satellite/back-trajectories/dispersion modelling information. These ratios  
512 have been shown previously to be rather robust indicators of the origin of mineral dust at the  
513 large scale (Formenti et al., 2011a and references therein). The result is shown in Figure 3.

514 There are some clear distinctions which that can be made. Data points having Si/Al > 3 are  
515 unambiguously identified as samples from the Bodélé depression, i.e. PSA 5. Their Fe/Ca

516 ratio is about 1. Data point having Fe/Ca > 3 are related to emission from erosive events in  
517 the Sahel. There are various sub-ranges in this group: data having Fe/Ca in the range 3–5  
518 correspond to transported dust aerosol from the Sahel, sampled 1–2 days after emission,  
519 corresponding to mixed sources, as PSA3 + Sahel. Data having Fe/Ca > 5 correspond to  
520 samples collected immediately or at the very early stage after emission by convective events,  
521 mostly locally at the ground-based Banizoumbou site (when the Fe/Ca ratio exceeds 10), but  
522 occasionally on uplifted dust onboard aircraft.

523 Data with Si/Al in the range 2.5–2.9 and Fe/Ca in the range 1–3 have their origins mostly at  
524 latitudes in the range 16–27°N, i.e. PSA 3. Whereas the variability of the Si/Al ratio is low,  
525 that of Fe and Ca can be used to make some distinctions amongst sources. Fe/Ca higher  
526 than 1 is measured for data points from northern Mali, Mauritania, Algeria, northern Niger  
527 and Libya whereas Fe/Ca < 1 is for dust from Western Sahara (PSA 2). For this source,  
528 there are two clear outliers corresponding to samples of dust originating from Morocco and  
529 showing the lowest Fe/Ca ratio (~ 0.4).

### 530 **3.2. Mineralogical composition**

531 The investigation of the mineral composition is based on 51 samples, 15 of which collected  
532 onboard aircraft. This dataset represents a diversity of sources and emission conditions.

533 The most evident peaks, for all samples, are those of illite, kaolinite and quartz. Less evident,  
534 and not ubiquitous, are the peaks corresponding to feldspars (albite and ortoclase), and  
535 calcium-rich minerals (calcite, dolomite, gypsum). Feldspars are found in the samples from  
536 local erosion and South Algeria/North Niger/Mauritania and Western Sahara. This last set  
537 might also contain calcium-rich minerals. Smectite clays are detected as a large and rather  
538 weak peak at angles comprised between 4 and 7°. This is indicative of the fact that smectites  
539 are a family of weathered clays of different chemical composition (e.g., montmorillonite,  
540 nontronite), whose crystalline structure can be heavily modified in the environment. Smectite  
541 clays were only evident in samples originated from South Algeria/North Niger/Mauritania and  
542 Western Sahara.

543 We can obtain the mass fractions of minerals which can be detected by X-ray diffraction by  
544 using the calibration factors as described in section 2.3.2 (Figure 4).

545 Regardless of the origin, clays and quartz account in average for 87% (± 6) and 10% (± 6) of  
546 the diffracting mass. There is only one clear outlier in an episode of intense local erosion  
547 sampled at the Banizoumbou super-site (sample SOP1-8), for which the percent clay fraction  
548 is reduced (56%), and the quartz and feldspars fraction enhanced (41% and 3.3%,  
549 respectively). This is consistent with the fact that at erosion the size distribution shows an



550 enrichment of coarse particles, whose composition should be closer to that of the soil silt  
551 fraction (Gillette and Walker, 1977; Chatenet et al., 1996).

552 The analysis of the XRD spectra also show that kaolinite and illite are very often the only clay  
553 species detected. A broad peak corresponding to smectites was detected on samples from  
554 Algeria and at times Bodélé, consistently with finding of Moreno et al. (2006). No chlorite has  
555 been detected in our samples. As explained in section 2.4.2.2, the relative proportions (by  
556 mass) of illite and kaolinite have been estimated using the origin-dependent ratios  
557 established by Caquineau et al. (2002). For the sources considered in this dataset, the illite-  
558 to-kaolinite ratios could vary between 0.1 and 2.3. The central and western Saharan sources  
559 (PSA2 and PSA3) display the highest values (1.6 to 2.3) for PSA 5, Northern Niger and  
560 Sahel the lowest values (0.1 to 0.7).

### 561 **3.3. Iron oxides content and speciation**

562 The quantification of the content of iron in the oxide form ( $\text{Fe}_{\text{ox}}$ ), that is free iron which is not  
563 in the crystal lattice of alumino-silicates, has been performed on 81 samples of different  
564 origins and load (33 out of those have been collected onboard aircraft). In average,  $\text{Fe}_{\text{ox}}$   
565 account for  $58 \pm 7\%$  of the mass of elemental Fe. The range of variability is illustrated in  
566 Figure 5.

567 The lowest values (down to 44%) are found for samples of dust originating from the PSA4  
568 (Chad/Egypt) area and for a set of samples collected above the PSA2 areas. The highest  
569 values (up to 71%) are obtained for samples of dust emitted by local erosion in the Sahel,  
570 including one episode in which uplifted dust has collected onboard aircraft after emission.  
571 Other subsets of samples, such as those of dust originated from the South Algeria/North of  
572 Niger areas, display equivalently high values when during long-range transport, dust from  
573 Algeria mixes with locally-produced dust in Niger. It should be noted also that, because of the  
574 internal variability of each group, there is no statistically-significant difference between the  
575 iron oxide fractions of the total iron for long-range transported dust originated at latitudes  
576 north of  $16^\circ\text{N}$ . A broad distinction between the  $\text{Fe}_{\text{ox}}$ -to-Fe ratio of Sahelian samples with  
577 respect to those of Saharan samples can be made by sorting the data points by their  
578 corresponding Fe/Ca ratio. Mineral dust emitted from the Sahel ( $\text{Fe}/\text{Ca} > 3$ ) are  
579 characterized by a mean  $\text{Fe}_{\text{ox}}$ -to-Fe ratio value of 65% ( $\pm 5\%$ , standard deviation of the  
580 mean), whereas episodes of transport from the Sahara ( $\text{Fe}/\text{Ca} < 3$ ) are characterized by a  
581 mean ratio of 56% ( $\pm 6\%$ ). No further distinction based on origin is possible in this second  
582 group of samples. This is illustrated in Figure 6.

583 X-ray absorption spectroscopy on twelve samples of differing origins indicated that goethite  
584 is overall the dominant species of iron oxides. Goethite accounts for 48 to 73% of the iron

585 oxide mass, whereas hematite accounts for 27 to 52%. These values do not show a clear  
586 trend with respect to the sample origin. The relative proportions of iron in the form of  
587 hematite and goethite with respect to total iron are shown in Table 2.

### 588 **3.4. Titanium oxides content**

589 Titanium oxides deserve attention as they are involved in photo-catalytical heterogeneous  
590 reactions with various atmospheric constituents, including volatile and semi-volatile organic  
591 compounds which are found in transport regions of mineral dust due to biomass burning  
592 emissions (Gustafsson et al., 2006).

593 We therefore examined our dataset in order to provide with estimates of the content of  
594 titanium oxides in mineral dust from various sources in western Africa. The titanium oxide  
595 content has been estimated from the measured element Ti concentration (obtained by XRF)  
596 which is converted to  $\text{TiO}_2$  using the appropriate molar mass conversion factor (1.67). This  
597 should be considered as an upper limit estimate as some of the titanium in mineral dust is  
598 present as substitution element in aluminosilicates (Dolcater et al., 1970).

599 Figure 7 presents the correlation between the  $\text{TiO}_2$  and the TDM. Two populations can be  
600 identified: one corresponding to samples collected in correspondence of erosion events and  
601 one corresponding to advection events. For both populations, the correlation is excellent ( $R^2$   
602 equal to 0.97 and 0.92, respectively) and the scatter of points is minimal. The  $\text{TiO}_2$  content is  
603 higher in erosion events from the Sahelian region (average 1.2% ( $\pm 0.1$ ) of the mass), than  
604 for advection events of Saharan dust, for which  $\text{TiO}_2$  represents in average 0.71% ( $\pm 0.01$ ) of  
605 the mass.

606 Looking at the elemental ratios between Ti, Fe, and  $\text{Fe}_{\text{ox}}$  provides with further insights  
607 (Figure 8). The ratio of Ti-to-Fe is insensitive to changes in the  $\text{Fe}_{\text{ox}}$  proportions to Fe up to  
608 60%, and then starts increasing linearly with increasing  $\text{Fe}_{\text{ox}}$ -to-Fe ratio. This suggests that,  
609 in Sahelian dust, Ti is associated with iron oxides but not in Saharan dust.

### 610 **3.5. Mass apportionment of the mineralogical composition**

611 By combining the information presented in section 3.1 to 3.4, we can estimate the  
612 mineralogical composition of samples of mineral dust of local or distant origin.

613 The mass apportionment is shown in Table 3. Note that we provide here with the  
614 composition of the bulk mineral dust, without explicitly taking into account the dependence on  
615 size.

616 There are clear similarities in the composition of the dust from those different origins, first of  
617 all in the fact that the clay fraction represents the largest fraction of the dust mass. Also note

618 the absence of Ca-rich minerals (calcite, dolomite, gypsum) in dust originating from the Sahel  
619 compared to that originated elsewhere.

620 Despite the overall similarities, there is indeed a large internal variability within each source  
621 group, expressed by the standard deviation around the mean, and which might be related to  
622 either the time or height after transport.

623 An example can be given by looking at the composition of the four samples in Bodélé/Sudan  
624 group: one sample was collected in the dry season, whereas the remaining three are  
625 sequenced samples collected in the wet season, at a time characterised by the absence of  
626 local emission, but by a progressively increasing entrainment of dust transported from the  
627 free troposphere to the surface layer (J. L. Rajot, pers. comm.). These wet-season samples  
628 have a lower clay fraction and a higher quartz and feldspar content (in the range 7–18% and  
629 0.4–0.8, respectively). This variability corresponds to differences in the volume size  
630 distribution, normalised to the total volume for sake of comparison (Figure 9). As a matter of  
631 fact, the volume size distribution of the dry-season sample presents a large coarse mode  
632 peaking around 4–5  $\mu\text{m}$ , whereas the wet-season samples have a bimodal volume size  
633 distribution with an additional mode centred at 8  $\mu\text{m}$ . Within this group, the sample having the  
634 largest quartz fraction is also the one displaying the larger fraction of particles above 10  $\mu\text{m}$ .

635 A second example of the links between time after emission, size distribution and  
636 composition, is given in Figure 10 showing the normalised particle size distributions (by  
637 volume) for one case of Sahelian dust by local erosion (sample SOP1-8), two samples  
638 representing the background dust composition in the absence of local erosion (SOP1-15 and  
639 SOP1-60) and one case representing the composition of Sahelian dust advected at the  
640 sampling site after having been emitted by local erosion in the proximity (SOP1-17). There  
641 are clear differences between these cases: sample SOP1-8 has a mode at 8  $\mu\text{m}$  and the  
642 largest coarse particle fraction. Samples SOP1-15 and SOP1-60 have a bimodal size  
643 distribution with modal diameters at 3–4 and 8  $\mu\text{m}$ . Finally, only the mode 3–4  $\mu\text{m}$  remains  
644 for sample SOP1-17. As for the case presented in Figure 9, it is evident from Figure 10 that  
645 the coarse mode at 8  $\mu\text{m}$  bears the most of the quartz and feldspar mass fractions, and that  
646 the dynamic evolution of this mode controls the content of quartz and feldspar in dust. The  
647 comparison of Figures 9 and 10 also suggests that, once the mode at 8  $\mu\text{m}$  is deposited,  
648 differences in the mineralogical composition of mineral dust will be more independent of the  
649 size dynamics and reflect better differences in the mineralogy of the parent soil.

## 650 **4. Discussion**

### 651 **4.1. Comparison with other datasets**

652 All comprehensive papers relating on the composition of mineral dust state that the  
653 comparison of compositional data from different datasets depends critically on the  
654 experimental conditions, in particular the duration and location of sampling (integration time,  
655 near-source location) (Formenti et al., 2011a; Scheuvens et al., 2013). These considerations  
656 are particular relevant to aircraft sampling where the difficulty in controlling the size cut-off of  
657 samplers generally disfavour the coarse particle fraction in an often non-quantified way  
658 (Formenti et al., 2011a). Furthermore, as the aircraft is moving during sampling, a 20-minute  
659 aircraft sample will represent a distance of the order of 120 km, which might integrate the  
660 contribution of various sources (Klaver et al., 2011).

661 As a consequence, the integration and the comparison of different datasets of the  
662 composition of mineral dust is not a straightforward exercise.

663 Overall, our results indicate the dominance of clays in the dust composition when only the  
664 aerosol fraction is measured. In this respect, they are in accordance with previously  
665 published papers for dust collected in Africa (Kandler et al., 2009) or after long range  
666 transport (Delany et al. 1967; Kiefert et al., 1996; Glaccum and Prospero, 1980; Caquineau  
667 et al., 2002). These measurements, however, tend to indicate that the clays fraction accounts  
668 for ~60-70% of the dust weight, whereas our measurements suggest higher values (80-90%).  
669 It should be reminded that the determination of the mineralogical composition will depend on  
670 the crystallography of the standard minerals used for calibration, and on the normalisation to  
671 the total dust mass. In our work the percentage of clays in dust depends directly on the  
672 normalisation factor, on which we have an uncertainty of the order of 17%, as we do estimate  
673 clays from the difference between the total dust mass and the calibrated mass of non-clay  
674 compounds. As an example, Glaccum and Prospero (1980), using standard clays minerals  
675 for calibration, estimate that the crystalline mass represented 70 to 110% of the weighed  
676 mass. These values reflect, at least partially, the uncertainty on the clay fraction.

677 Nonetheless, in some cases differences might be due to sampled aerosol size distribution.  
678 As a matter of fact, the lowest detected percentage of clays corresponds to sample SOP1-8,  
679 collected during an intense episode of local erosion. In this case, clays account for around  
680 50% of the measured mass, in accordance with measurements by Caquineau et al. (1997;  
681 2002) in similar conditions.

682 This is also clear for example by looking at the data published by Kandler et al. (2009), who  
683 documented the dust composition in dust storm (total suspended particulate concentrations  
684 higher than  $300,000 \mu\text{g m}^{-3}$ ) and low dust periods (total suspended particulate

685 concentrations around  $100 \mu\text{g m}^{-3}$ ) in Morocco. Quartz accounts for as high as ~65% in dust  
686 storm conditions, suggesting that soil grains, and not only aerosols, were sampled.  
687 Conversely, low-dust conditions are characterised by only about 20% of quartz. These  
688 authors showed that, for locally emitted dust, illite is the dominant clay form over kaolinite (up  
689 to 30 and 5% by volume, respectively). These authors also detected clay in the form of  
690 chlorite (less than 10% by weight) and calcite (up to 15%).

691 Few authors have published data on the iron oxide content. Lafon et al. (2004) evaluated the  
692 free-to-total iron content in samples collected at the Banizoumbou ground-based site and  
693 found mean values of  $0.44 (\pm 0.11)$  and  $0.65 (\pm 0.04)$  for dust transported in the Harmattan  
694 flow (from the Sahara) and dust emitted locally by convective erosion. Lazaro et al. (2008)  
695 found sensibly lower values than ours ranging from 0.26 to 0.63 but only exceeding 0.56 in  
696 three occasions when back-trajectories indicated transport from the Sahel or a mixture of  
697 dust originating from the Sahara and the Sahel. Our values are on the higher side with  
698 respect to those of these authors. Nonetheless, the back-trajectories presented in the paper  
699 seem indicating that the Saharan dust originated from higher latitudes than the one we  
700 sampled – and mostly from Tunisia and Algeria. It will be interesting in the future to sample  
701 those source areas to confirm these rather low values.

702 Finally, our results on the iron oxide speciation are consistent with findings of different  
703 authors using XANES speciation (Wilke et al. 2001; Ohta et al., 2006; Prietzel et al. 2007;  
704 Majestic et al., 2007) and visible spectroscopy (Arimoto et al., 2002) indicating that Fe(III) is  
705 the dominant red-ox form of iron oxides and that goethite is the predominant form of iron  
706 oxide over hematite.

## 707 **4.2. Atmospheric implications**

708 The results showed in this paper suggest that, when restricted to the mass fraction below 20  
709  $\mu\text{m}$ , the dust composition in western Africa may apparently be simplified to few minerals,  
710 clays, quartz, calcite, iron and titanium oxides. Feldspars and other calcium-containing  
711 minerals such as dolomite and gypsum are very minor components close to detection limits.  
712 The geographical distribution of the dust composition is relatively unimportant in terms of  
713 mass fractions, in particular in comparison to the importance of the size distribution whose  
714 variability with time seems to be able to explain some differences observed between samples  
715 from the same source region at different times after emission. Nonetheless, it is important to  
716 evaluate whether differences in the composition at the regional scale, even when minor,  
717 might give rise to differences in the impacts of mineral dust.

718 To do so, we explore the influence of dust composition on the spectral complex refractive  
719 index  $\tilde{n}$  and the fraction iron solubility.

#### 720 **4.2.1. Implications for optical properties**

721 As a mean of evaluating the effect of the variability of the composition on the dust optical  
722 properties, the volume-average refractive index has been calculated as

723

$$724 \quad \tilde{n} = \sum_j f_j \times \tilde{n}_j \quad (4)$$

725

726 where  $f_j$  is the volume fraction of each individual mineral in the dust sample (as reported in  
727 Table 3) and  $\tilde{n}_j$  is its complex refractive index. Equation 4 assumes that minerals in dust are  
728 in internal mixing. In reality, minerals are present in dust as external mixtures, with the  
729 exception of iron oxides which may be found as inclusions in clays (Sokolik and Toon, 1999).  
730 However, the internal mixing hypothesis is frequently used in experiments and climate  
731 models (e.g., Balkanski et al., 2007; Kandler et al., 2009; McConnell et al., 2010; Hansell et  
732 al., 2011),

733 Values of the complex refractive index  $\tilde{n}_j$  of the individual minerals detected in our samples  
734 are listed in Table 4. We have restricted the calculations to two spectral domains: the near  
735 UV-visible between 370 and 700 nm and the thermal IR from 8 to 15  $\mu\text{m}$ , where values for all  
736 individual minerals are available.

737 Results are presented in Figure 11, where they are compared to the values of the “desert”  
738 dust aerosol model in the OPAC (Optical Properties of Aerosols and Clouds) database (Hess  
739 et al., 1998), often used in satellite retrieval algorithms in the thermal infrared (see Table 1 in  
740 Klüser et al., 2012), but also in radiative transfer calculations (Highwood et al., 2003;  
741 Haywood et al., 2005). The “desert” model in the OPAC database represents the properties  
742 of mineral dust at source region, considered as a mixture of quartz and clays in different size  
743 fractions.

744 We restrict Figure 11 to the visible and infrared imaginary parts of the complex refractive  
745 index  $\tilde{n}_i$ . In the visible, the imaginary part of the complex refractive index is relatively  
746 constant with wavelength. Mean values are of the order of 0.003, with standard deviation of  
747 the order of 0.001, with the exception of data from the PSA4 source, which average at 0.006  
748 and present a standard deviation (0.003). It is difficult to judge on this variability as it is  
749 induced by one sample only presenting an outstanding iron oxide fraction. In the infrared, the  
750 imaginary part shows a band-type structure in correspondence to the major absorption bands  
751 of clays and quartz, mostly found in the atmospheric window between 8 and 11  $\mu\text{m}$ . There is  
752 very little sample-to-sample variability in the position of the bands, as well as in the relative  
753 proportions of the band peaks, with the exception of the Sahelian dust samples, which

754 present a larger standard deviation due to the enhancement of the band at 9.2  $\mu\text{m}$   
755 corresponding to the outstanding quartz fraction of sample SOP1-8. There is very little  
756 difference in the spectra of sources PSA3, PSA4 and to a lesser extent PSA5, which have  
757 the highest absorption values at 9.6  $\mu\text{m}$ . However, the spectral dependence for dust from  
758 source PSA2 is different (peak at 9.2  $\mu\text{m}$  more pronounced than that at 9.6  $\mu\text{m}$ ).

759 The composition-based refractive indices calculated in this work are very different to those of  
760 the OPAC database. Below 0.6  $\mu\text{m}$ , the volume-averaged values are on the lower side than  
761 the OPAC values, with the exception of values for the PSA4 samples, due to their larger  
762 standard deviation. Above, the two datasets approach. The spectral dependence is also  
763 inconsistent, and reflects the reduced spectral variability of the values for iron oxides (both  
764 hematite and goethite) in Bédidi and Cervelle (1993) with respect to other commonly used  
765 databases, such as that of Shettle (1979) for hematite on which OPAC is based.

766 The calculated volume-average infrared values in the absorption band between 8 and 10  $\mu\text{m}$   
767 are two times higher than in the OPAC database. The main reason for that is the volume-  
768 mixing rule which enhances absorption. Additionally, for single-mineral species, various  
769 authors (Hudson et al. 2008a, 2008b; Mogili et al., 2007, 2008) found strong differences in  
770 peak positions and spectral shape between extinction spectra measured by Fourier-  
771 transform infrared spectrometry and those calculated from published optical constants. All  
772 these studies show residual differences suggesting that optical constants might vary  
773 depending on whether they had been determined on powders or bulk samples, on the  
774 degree of water association of minerals, and on their chemical form (substitutions,  
775 impurities). As this variability might be even larger when looking at actual dust samples, the  
776 comparison clearly suggests that new measurements of IR extinction spectra on real dust  
777 samples representative of the mineralogical composition of the different source areas are  
778 required.

#### 779 **4.2.2. Implications for Fe fractional solubility**

780 The solubility of dust iron is a function of iron speciation, i.e. oxidation states, bonding  
781 environments and mineralogy (Journet et al., 2008; Schroth et al., 2009). Thus, due to higher  
782 solubility of iron trapped in the crystal lattice of aluminosilicates and the large abundance of  
783 clay minerals, Journet et al. (2008) suggested that the use of hematite as a single source of  
784  $D\text{Fe}$  in biogeochemical models might cause an underestimation of the  $D\text{Fe}$  supply to the  
785 ocean. On this assumption, Paris et al. (2011) showed that the iron fractional solubility from  
786 analogue of mineral dust can be estimated as the sum of Fe solubility of various minerals  
787 compounding iron in the dust matrix. We propose to apply this calculation to this dataset to  
788 estimate the solubility of dust in source region. For this purpose, we use the iron solubility

789 from minerals measured by Paris et al. (2011) at pH = 4.7 which a typical pH of African  
790 rainwaters (Desboeufs et al., 2010), i.e.  $S_{Fe}$  equal to 0.17% for illite and 0.006% for free iron  
791 from goethite and hematite. Paris et al. (2011) made the approximation that all the iron  
792 associated to clay is present as illite. Journet et al. (2008) emphasized that even the iron in  
793 impurities into kaolinite or feldspars matrix present a high solubility. Our measurements show  
794 the predominance of kaolinite in comparison to illite, so we consider also the dissolution of  
795 Fe from kaolinite due to the large proportion of this mineral in the studied samples. We use a  
796  $S_{Fe} = 0.63\%$  for kaolinite (Paris, personal communication). The percent quantity of feldspar  
797 being usually inferior to 1% in the samples, we neglect the iron associated to these minerals.  
798 Smectites, such as montmorillonite, are also minerals with high content of iron with a higher  
799 solubility (Journet et al., 2008). However, due to the difficulties in quantifying the smectite  
800 fraction, this other source of structural Fe is not well constrained. Moreover, Shi et al. (2011)  
801 mention the presence of highly-soluble nanoparticles of ferrihydrite or poorly crystallized iron  
802 in fine fraction of soils. However, the quantification of this iron phase is obtained by  
803 sequential extraction and is difficult to apply on field samples due to the low mass. So we are  
804 not able to consider this species in our calculation.

805 Among the samples present in our database, the mineralogical composition including  
806 goethite, hematite, illite and kaolinite is evaluated for 27 samples, enabling to calculate the  
807 iron fractional solubility (Table 3). In this case, the iron content in illite is assumed equal to  
808  $4.0 \pm 0.9\%$ , which corresponds to the mean stoichiometric value of two types of illites  
809 (Fithian, Illinois and Rochester, Minnesota, as shown in Journet et al., 2008). The iron  
810 content in illite can vary from 0.8% to 8.4 % (Murad and Wagner, 1994), this large range is  
811 due to the fact that Fe is present as substitution of Al or K in the sheet-like structure of illite,  
812 and this will depend on the environmental conditions that the clay has experienced in the soil  
813 fraction (weathering,...). In goethite and hematite, we estimated the iron content based on the  
814 analysis of Journet et al. (2008) and Paris et al., (2011) as 62.9% and 57.5% for goethite and  
815 hematite, respectively. For kaolinite, Mestdagh et al. (1980) show that the iron content is  
816 related to the cristallinity of the mineral and ranges from 0.02% to 0.81% with an average of  
817  $0.4\% \pm 0.2\%$ , which is used for our calculation.

818 In order to have a larger view of the variability of iron solubility as a function of emission  
819 source, we can also calculate iron solubility from the partitioning between structural and free  
820 iron as obtained by the CBD extraction analysis (Table 2). This is doable for 85 samples,  
821 among which the 27 samples for what the mineralogical composition is estimated. In this  
822 case, we consider the structural iron ( $\%Fe_{\text{structural}}$ ) is associated to illite ( $\%Fe_{\text{illite}}$ ) and kaolinite  
823 ( $\%Fe_{\text{kaolinite}}$ ) in the proportion of illite-to-kaolinite ratio corresponding to the origin of the  
824 samples (see 3.2), such as:



$$\%Fe_{kaolinite} = \frac{\%Fe_{structural}}{\left(1 + 10 \times \frac{I}{K}\right)}$$

825 and  $\%Fe_{illite} = \%Fe_{structural} - \%Fe_{kaolinite}$

826

827 with 10 represents the illite-to-kaolinite iron content ratio (4.0%/0.4%)

828 Results are summarized in Figure 12.

829 The mean value of iron fractional solubility is 0.10% ( $\pm 0.02\%$ ) whatever the methods of  
 830 calculation, i.e. from mineralogical composition or from CBD extraction analysis. There is  
 831 little variability of iron solubility as a function of the source; nonetheless, this is directly  
 832 opposite to the iron oxide content, i.e., the lowest values ( $0.08\% \pm 0.01\%$ ) obtained for  
 833 samples of dust emitted by local erosion in the Sahel, in agreement with the highest iron  
 834 oxides content. Inversely, the samples with the highest solubility ( $0.13\% \pm 0.01\%$ ) issued  
 835 from PSA3, i.e. South Algeria/Mali which present a low % of free iron (49%). Data show that  
 836 54 to 87% of soluble iron is structural iron associated to illite, meaning that this mineral is the  
 837 major provider of soluble iron in our conditions of calculation. The determining factor for this  
 838 parameter is the quantification of illite and hence the hypothesis made on the illite-to-kaolinite  
 839 ratio as a function of emission source, which is estimated from Caquineau et al. (2002).  
 840 Thus, the regional variability on iron solubility obtained here is mainly associated with this  
 841 ratio which should be better constrained. A rapid calculation for the PSA3 samples, the  
 842 richest in structural iron, show that the iron solubility is divided by a factor 2 when I/K varies  
 843 from 0.1 to 2.3, the extreme values observed by Caquineau et al. (2002). This means that  
 844 the solubility between the various emission sources varies at the best by a factor 2. Another  
 845 source of error could be the estimation of iron oxide which is affected by 30% errors (and  
 846 those of illite too, by extension). Sample-to-sample comparison shows that there is a rather  
 847 good correspondence with the two methods of calculation (within 15%). However, the  
 848 calculation based on mineralogy yields values lower by a factor of 1.5 for the samples issued  
 849 from PSA3 alone or in mixing with other sources, meaning an underestimation of structural  
 850 iron in comparison from the direct measurements by CBD analyses. Smectites are identified  
 851 for several samples of this source, we underestimate so the calculated solubility for the  
 852 samples where these minerals are present.

853 The mean fractional iron solubility obtained by calculation is consistent but rather inferior to  
 854 the observations obtained for transported Saharan dust over Atlantic which ranges from 0.12  
 855 to 4.1% (Sarhou et al., 2003; Baker et al., 2006; Sholkovitz et al., 2012). However, our  
 856 calculation are exclusively based on mineralogical parameters, since our samples have been

857 collected at most 2 days after emission and do not integrate the various chemical and  
858 physical processes increasing dust solubility during long range transport, as cloud process  
859 (Desboeufs et al., 2001); photochemical process (Hand et al., 2004) or organic complexation  
860 (Paris et al., 2013). Thus, the range of calculated values could be representative of iron  
861 solubility for the various sources of African dust before transport. Moreover, the limited  
862 regional variability estimated here in comparison to the variability of measurements over  
863 Atlantic Ocean show that the emission source of dust is less critical than the process after  
864 transport to estimate the fractional iron solubility of dust. Nevertheless, new direct  
865 measurements of the iron fractional solubility for sources of dust in Western Africa are  
866 necessary to validate these conclusions.

## 867 **5. Final remarks, conclusions and perspectives**

868 In this paper we have presented an insight on the mineralogical composition of mineral dust  
869 from Western Africa from the synthesis of the airborne and ground-based observations of  
870 field campaigns conducted between 2006 and 2007. These observations have been  
871 performed at emission or within 2 days of transport in the atmosphere. The strength of this  
872 synthesis resides in the fact that the observations have been performed in a consistent way  
873 from the methodological point of view (both for the sample collection and analysis) and that  
874 they span a large geographical region covering some of the major African dust sources.

875 The composition data presented in this paper are being made public on a dataset called  
876 DUST-MAP, to date still on its trial version. Meanwhile, data are available upon request. The  
877 perspective evolution of this dataset will be the inclusion of data from other field campaigns,  
878 both close to source regions and at some distance. Amongst those are the FENNEC and the  
879 SAMUM field campaigns (Heintzenberg et al., 2008; Ansmann et al., 2011; Washington et  
880 al., 2013), which were conducted downwind sources in Algeria and Morocco relevant to  
881 large-scale transport (Caquineau et al., 2002). This will require a close-up examination of  
882 experimental protocols and a careful evaluation of their influence on the results.

883 The presentation of this work deserves some final considerations and opens various  
884 perspectives.

885 The bulk mineralogical composition of dust in Western Africa can be described by a simple  
886 model where kaolinite and illite account for 80% or above of the mass, and quartz, iron and  
887 titanium oxides for the remaining 20%. Calcite is a distinctive element of Saharan sources for  
888 which it ranges between 0.3 and 8.4% in dust mass. For the remaining minerals, the  
889 variability is due to source type (e.g., the proportions of illite and kaolinite as evidenced by  
890 Caquineau et al. (2002)) or to differences in the size distribution, particularly the increase of  
891 the quartz fraction corresponding to a coarse mode centred around 8  $\mu\text{m}$  in diameter. For the

892 first time to our best knowledge, we provide with a large dataset of titanium oxide data which  
893 can be relevant to atmospheric photochemistry (N'Dour et al., 2009). We estimate that  
894 Sahelian dust is composed by 2% (by mass) of titanium oxides, that is, double the mass  
895 fraction of dust from sources in the PSA2, PSA3, PSA4 and PSA5 areas, with very little  
896 sample-to-sample variability. Iron oxides, also important for atmospheric chemistry  
897 processes and radiation, display higher values in Sahelian than in Saharan dust.

898 The discussion of the regional variability of the mineralogical composition is based on our  
899 ability in detecting source areas based on satellite remote sensing or on soil properties map  
900 (e.g., Claquin et al., 1999; Schepanski et al., 2007; Laurent et al., 2008; Ginoux et al., 2012;  
901 Nickovic et al., 2013; Journet et al., 2014), and in attributing the provenience of an air mass  
902 to it via back-trajectory calculations (e.g., Klaver et al., 2011). Beside the uncertainties  
903 inherent to the detection of sources, there are two additional factors of ambiguity in source  
904 attribution: first, air masses, especially during winter-time, mostly travel in the boundary layer  
905 and might uplift dust aerosols at various times before reaching the sampling site; secondly,  
906 aircraft samples might integrate transport from various sources active at the same time due  
907 to the fact that aircraft moves during sampling and that sample collection lasts at least 20  
908 minutes, which corresponds to about 120 km at typical aircraft cruise speed (see Figure 1 in  
909 Chou et al., 2008 and Figure 1 in Klaver et al., 2011). It is therefore clear that some fine  
910 features of the mineralogy specific to individual sources might be lost. Nevertheless, our data  
911 well represent the composition of the regional dust load as it results from the natural mixing  
912 occurring during transport. They are also of comparable spatial resolution to that of various  
913 state-of-the-arts global and regional circulation models including dust mineralogy (Balkanski  
914 et al., 2007; Hoose et al., 2008; Huneeus et al., 2010). Henceforth, the composition data  
915 presented in this paper may serve to evaluate the regional and global model estimates of the  
916 dust mineralogical composition in the Western African atmosphere and to calculate dust  
917 properties relevant to their direct, indirect and biogeochemical impacts. Claquin et al. (1999)  
918 have discussed some comparisons between the mineralogy of dust atmospheric data and  
919 that of the soil fraction predicted by a surface mineralogy table constructed from maps of the  
920 arid soil mineralogy (updates of this table have been recently published by Nickovic et al.  
921 (2012) and Journet et al. (2014)). To do so, these authors have calculated weight ratios  
922 between some minerals (calcite, feldspar and hematite, where hematite is meant to  
923 represent the sum of the content of goethite and hematite) with respect to quartz. Our data  
924 are consistent with the Claquin et al. (1999) dataset regarding the variability of the calcite-to-  
925 quartz ratio, but display higher and lower ratios for hematite and feldspar, respectively. Our  
926 ratio of hematite-to-quartz ranges between 0.03 and 1 (0.09 and 3 when the sum of goethite  
927 and hematite is considered) instead than 0.009–0.09, whereas our ratio feldspar-to-quartz is

928 in the range 0.03–0.11 instead that 0.2–2 in Claquin et al. (1999). These differences illustrate  
929 the fact that our data are closer to representing the clay soil fraction, whereas the data of  
930 Claquin et al. (1999) best represent also the silt fraction, richer in quartz particles. When  
931 limited to sample SOP1-8, the local erosion sample enriched in quartz and in the particle  
932 fraction larger than 20  $\mu\text{m}$ , ratios are 0.09 for hematite-to-quartz (0.03 if hematite only is  
933 considered) and 0.08 for feldspar-to-quartz, in the range expressed by Claquin et al. (1999).

934 Finally, we have provided with the estimate of parameters relevant to the direct impact of  
935 mineral dust on radiation and on ocean productivity: the complex refractive index  $\tilde{n}$  and the  
936 iron fractional solubility  $S_{\text{Fe}}$ .

937 Assuming internal mixing, we have shown that the complex index of refraction based on  
938 mineralogy has some variability mostly related to the partitioning between illite and kaolinite  
939 and to the quartz fraction higher than 40% of the dust volume. The spectral behaviour of the  
940 estimated complex index of refraction is quite different from the OPAC database. The OPAC  
941 approach overestimates absorption in the visible. On the other hand, a very recent study  
942 presents values of the complex refractive index in the shortwave based on a global  
943 mineralogy soil map (Schmid et al., 2013). At 550 nm, these authors predict a real part of the  
944 complex refractive index around 1.56, that is, higher than our which ranges between 1.45  
945 and 1.51. Their imaginary part averaging at  $6.2 \times 10^{-4}$ , that is, almost an order of magnitude  
946 lower than our predicted values (average  $3 \times 10^{-3}$ ). This is the consequence of the fact that  
947 optical properties estimated from the soil fraction will reflect more closely the optical  
948 properties of quartz, which, is enriched in the soil fraction but which in the aerosol fraction  
949 due to the size fractionation at emission. An additional confirmation is given by the fact that,  
950 in our data, the highest value of the real part of the complex refractive index is obtained for  
951 sample SOP1-8, representing the Sahelian erosion case with the highest quartz fraction  
952 (41% by weight), whereas the highest values of the imaginary part are obtained for samples  
953 representing long-range transport from Libya through north Niger, having a low or even the  
954 lowest quartz percentage by weight (1.5–6%) but having the highest calcite fraction (4–8%  
955 by weight). As a matter of fact, quartz is transparent in the visible, whereas calcite, but also  
956 clays are absorbing. These considerations bring to the conclusion that not only the soil  
957 mineralogy but also the transfer function between the soil and the aerosol fractions must be  
958 implemented in models estimating the dust optical properties.

959 In the longwave spectrum, our calculations suggest higher absorption than the OPAC model  
960 in the atmospheric window. The 10–12  $\mu\text{m}$  band, which is sensitive to differences in the  
961 mineralogical composition amongst sources, is relevant to the retrieval of various space-  
962 borne sensors, including IASI, AIRS, and MODIS (De Souza Machado et al., 2006; Hudson  
963 et al., 2008; Klüser et al., 2011; Laskina et al., 2012). Some of the discrepancies between

964 our values and the OPAC database to be, at least partially, due to differences in the optical  
965 constants of the individual minerals. Dedicated in situ measurements of the optical constants  
966 of the dust samples would allow confirming this hypothesis.

967 Nonetheless, a limitation of this work, impacting our estimate of the complex refractive index,  
968 is the quantification of smectite-type clays. For the purposes of the present study, we have  
969 chosen to neglect the contribution of smectites, which were detected only on a few samples,  
970 and which we consider as a trace component of the aerosol. Also, smectites are dominant in  
971 the 0.2  $\mu\text{m}$  size fraction, which is poor in mineral dust in our samples (Klaver, 2012).

972 In the visible Egan and Hilgeman (1979) indicated that two different montmorillonite types  
973 (one from Wyoming and one from Mississippi) have very similar refractive indices, to those of  
974 either kaolinite or illite, both in spectral dependence and magnitude. However, below 500 nm  
975 the imaginary part of the complex refractive index of the montmorillonite from Mississippi is  
976 higher by a factor of 2 than that of illite, reaching 0.004 between 200 and 360 nm. In the  
977 infrared, various authors (Toon et al., 1976; Glotch et al., 2007; Hudson et al., 2008) have  
978 shown that montmorillonite has similar optical properties to those of illite, albeit displaying  
979 higher intensity of extinction around 9.5  $\mu\text{m}$ , in the Si–O stretching band. Köster et al. (1999)  
980 examined 5 types of nontronites and Fe-rich smectites and found that the position and the  
981 intensity of this band vary depending on tetrahedral Fe(III) content. Also, the speciation of  
982 clays, in particular that of montmorillonite, has implications for the cloud and ice nucleation  
983 properties of mineral dust and the estimate of iron fractional solubility (Hoose et al., 2008;  
984 Journet et al., 2008). Ultimately, these facts depend on the compositional heterogeneity in Al-  
985 rich smectite in the natural soils and sediments (Christidis and Dunham 1993, 1997;  
986 Christidis, 2006), due to various processes, including weathering and/or hydrothermal  
987 alteration of basic rocks (Köster et al. 1999), but also reduction reactions of structural Fe by  
988 microorganisms (Pentakovska et al., 2013). This makes their quantification extremely  
989 dependent on the environmental conditions. Similar considerations will hold for chlorite-type  
990 clays, which were not detected in our samples, but might be present in dust from North  
991 African deserts such as Morocco and Tunisia (Paquet et al., 1984; Kandler et al., 2009). It  
992 should be noted that to date no measurements of the complex refractive index of chlorites  
993 are available in the shortwave. In the longwave, chlorite has significantly different optical  
994 properties than illite and kaolinite, in particular concerning their major absorption bands,  
995 which is located at 9.6  $\mu\text{m}$  for illite and kaolinite, and at 10.2  $\mu\text{m}$  for chlorite (Egan and  
996 Hilgeman, 1979; Mooney and Knacke, 1985). Should chlorite be detected in the samples, its  
997 lack of quantification will be treated as an additional source of error to be evaluated.

998 Regarding the iron fractional solubility, our data are not conclusive in identifying a clear  
999 regional difference with respect to the variability observed for dust collected over the Atlantic

1000 Ocean after short- and long-range transport. This limited regional variability suggests that a  
1001 single reference value (0.1%) of the fractional solubility  $S_{Fe}$  of Saharan and Sahelian dust  
1002 before atmospheric transport could be used in biogeochemical models. Direct field  
1003 measurements of  $S_{Fe}$  close to emission sources, unavailable at the moment, are needed to  
1004 confirm this finding. Finally, the  $S_{Fe}$  value estimated for dust near source regions is in the  
1005 lowest range than values obtained for dust collected over the Atlantic Ocean, pointing to the  
1006 need of taking atmospheric processing into account when iron solubility is ought to be  
1007 described at the global scale.

## 1008 **Acknowledgements**

1009 This research was funded by several institutions. Based on a French initiative, AMMA was  
1010 built by an international scientific group and is currently funded by a large number of  
1011 agencies, especially from France, the United Kingdom, the United States, and Africa. It has  
1012 been the beneficiary of a major financial contribution from the European Community's Sixth  
1013 Framework Research Programme. Detailed information on scientific coordination and  
1014 funding is available on the AMMA International Web site at [www.amma-international.org](http://www.amma-international.org).  
1015 Financial support by the API-AMMA and LEFE (project BIRD) French national funding  
1016 programs is also acknowledged. The participation of P. Formenti to the DODO and GERBILS  
1017 field campaigns was supported and by the UK NERC and by the UK MetOffice, which are  
1018 gratefully acknowledged.

1019 Thanks are also due to the LISA personnel who participated in field campaigns and helped  
1020 with sample collection, as well as to the BAe-146 and SAFIRE air and ground crews, as well  
1021 as the FAAM and Met Office observers.

1022

## 1023 **References**

1024 Abdourhamane Toure, A., Rajot J.L., Garba, Z., Marticorena, B., Petit, C., Sebag, D.  
1025 2011 Impact of very low crop residues cover on wind erosion in the Sahel. *Catena*, 85:205-  
1026 214. doi:10.1016/j.catena.2011.01.002.

1027 Alfaro, S. C., Gaudichet, A., Gomes, L., and Maillé, M.: Mineral aerosol production by  
1028 wind erosion: aerosol particle sizes and binding energies., *Geophys. Res. Lett.*, 25, 991-994,  
1029 1998.

1030 Andreae, M. O., Berresheim, H., Andreae, T. W., Kritz, M. A., Bates, T. S., and  
1031 Merrill, J. T.: Vertical distribution of dimethylsulfide, sulfur dioxide, aerosol ions, and radon  
1032 over the Northeast Pacific ocean, *J. Atmos. Chem.*, 6, 149-173, 1988.

1033 Ansmann, A., Petzold, A., Kandler, K., Tegen, I. N. A., Wendisch, M., Müller, D.,  
1034 Weinzierl, B., Müller, T., and Heintzenberg, J.: Saharan Mineral Dust Experiments SAMUM-  
1035 1 and SAMUM-2: what have we learned?, *Tellus B*, 63, 403-429, 10.1111/j.1600-  
1036 0889.2011.00555.x, 2011.

- 1037 Arimoto, R., Balsam, W., and Schloesslin, C.: Visible spectroscopy of aerosol  
1038 particles collected on filters: iron-oxide minerals, *Atmospheric Environment*, 36, 89-96, 2002.
- 1039 Atkinson, J. D., Murray, B. J., Woodhouse, M. T., Whale, T. F., Baustian, K. J.,  
1040 Carslaw, K. S., Dobbie, S., O'Sullivan, D., and Malkin, T. L.: The importance of feldspar for  
1041 ice nucleation by mineral dust in mixed-phase clouds, *Nature*, 498, 355-358,  
1042 10.1038/nature12278, [http://www.nature.com/nature/journal/v498/n7454/abs/nature12278.ht](http://www.nature.com/nature/journal/v498/n7454/abs/nature12278.html#supplementary-information)  
1043 [ml#supplementary-information](http://www.nature.com/nature/journal/v498/n7454/abs/nature12278.html#supplementary-information), 2013.
- 1044 Balkanski, Y., Schulz, M., Claquin, T., and Guibert, S.: Reevaluation of Mineral  
1045 aerosol radiative forcings suggests a better agreement with satellite and AERONET data,  
1046 *Atmos. Chem. Phys.*, 7, 81-95, 10.5194/acp-7-81-2007, 2007.
- 1047 Baron, P. A., and Willeke, K.: *Aerosol measurement: Principles, techniques and*  
1048 *applications*, 2nd ed., John Wiley and Sons, New York, 2001.
- 1049 Barthelmy, D., *Mineralogy database*. Available at <http://www.webmineral.com>, 2007.
- 1050 Bedidi A et Cervelle B., Light scattering by spherical particles with hematite and  
1051 goethite like optical properties : Effect of water impregnation. *J. Geophys. Res.*, 98, 11,941-  
1052 11,952, 1993.
- 1053 Ben-Ami, Y., Koren, I., and Altaratz, O.: Patterns of North African dust transport over  
1054 the Atlantic: winter vs. summer, based on CALIPSO first year data, *Atmos. Chem. Phys.*, 9,  
1055 7867-7875, 10.5194/acp-9-7867-2009, 2009.
- 1056 Ben-Ami, Y., I. Koren, Y. Rudich, P. Artaxo, S. T. Martin, and M. O. Andreae,  
1057 Transport of North African dust from the Bodélé depression to the Amazon Basin: a case  
1058 study, *Atmos. Chem. Phys.*, 10, 7533–7544, 2010.
- 1059 Boucher, O., D. Randall, P. Artaxo, C. Bretherton, G. Feingold, P. Forster, V.-M.  
1060 Kerminen, Y. Kondo, H. Liao, U. Lohmann, P. Rasch, S.K. Satheesh, S. Sherwood, B.  
1061 Stevens and X.Y. Zhang, 2013: Clouds and Aerosols. In: *Climate Change 2013: The*  
1062 *Physical Science Basis. Contribution of Working Group I to the Fifth Assessment Report of*  
1063 *the Intergovernmental Panel on Climate Change* [Stocker, T.F., D. Qin, G.-K. Plattner, M.  
1064 Tignor, S.K. Allen, J. Boschung, A. Nauels, Y. Xia, V. Bex and P.M. Midgley (eds.)].  
1065 Cambridge University Press, Cambridge, United Kingdom and New York, NY, USA.
- 1066 Bristow, C. S., Drake, N., and Armitage, S.: Deflation in the dustiest place on Earth:  
1067 The Bodélé Depression, Chad, *Geomorphology*, 105, 50-58,  
1068 <http://dx.doi.org/10.1016/j.geomorph.2007.12.014>, 2009.
- 1069 Brooks, N., and Legrand, M.: Dust variability over North Africa and rainfall in the  
1070 Sahel, in: *Linking climate change to land surface change, Advances in Global Change*  
1071 *Research*, Kluwer Academic Publishers, Dordrecht, 1-25, 2003.
- 1072 Caquineau, S., M.-C. Magonthier, A. Gaudichet, and Gomes, L.: An improved  
1073 procedure for the X-ray diffraction analysis of low-mass atmospheric dust samples, *Eur. J.*  
1074 *Mineral.*, 9, 157- 166, 1997.
- 1075 Caquineau, S., Gaudichet, A., Gomes, L., and Legrand, M.: Mineralogy of Saharan  
1076 dust transported over northwestern tropical Atlantic Ocean in relation to source regions, *J.*  
1077 *Geophys. Res.*, 107, 4251, 10.1029/2000jd000247, 2002.
- 1078 Carslaw, K. S., Boucher, O., Spracklen, D. V., Mann, G. W., Rae, J. G. L., Woodward,  
1079 S., and Kulmala, M.: A review of natural aerosol interactions and feedbacks within the Earth  
1080 system, *Atmos. Chem. Phys.*, 10, 1701-1737, doi:10.5194/acp-10-1701-2010, 2010.
- 1081 Chatenet, B., B. Marticorena, L. Gomes, and G. Bergametti, Assessing the microped  
1082 size distributions of desert soils erodible by wind, *Sedimentology*, 43, 901, 1996.
- 1083 Chou, C., Formenti, P., Maille, M., Ausset, P., Helas, G., Harrison, M., and Osborne,  
1084 S.: Size distribution, shape, and composition of mineral dust aerosols collected during the

- 1085 African Monsoon Multidisciplinary Analysis Special Observation Period 0: Dust and Biomass-  
1086 Burning Experiment field campaign in Niger, January 2006, *J. Geophys. Res.*, 113, D00C10,  
1087 10.1029/2008jd009897, 2008.
- 1088 Christidis, G. E., Genesis and compositional heterogeneity of smectites. Part III:  
1089 Alteration of basic pyroclastic rocks—A case study from the Troodos Ophiolite Complex,  
1090 Cyprus, *American Mineralogist*, Volume 91, pages 685–701, 2006
- 1091 Christidis, G. E. and Dunham, A.C., Compositional variations in smectites: Part I.  
1092 Alteration of intermediate volcanic rocks. A case study from Milos Island, Greece. *Clay*  
1093 *Minerals*, 28, 255–273, 1993.
- 1094 Claquin, T., Schulz, M., and Balkanski, Y. J.: Modeling the mineralogy of atmospheric  
1095 dust sources., *J. Geophys. Res.*, 104, 22243-22256, 1999.
- 1096 Crowley, J. N., Ammann, M., Cox, R. A., Hynes, R. G., Jenkin, M. E., Mellouki, A.,  
1097 Rossi, M. J., Troe, J., and Wallington, T. J.: Evaluated kinetic and photochemical data for  
1098 atmospheric chemistry: Volume V: heterogeneous reactions on solid substrates, *Atmos.*  
1099 *Chem. Phys.*, 10, 9059-9223, 10.5194/acp-10-9059-2010, 2010.
- 1100 Cullen, M. J. P., The unified forecast/climate model. *Meteorol. Mag.* 122: 81–93,  
1101 1993.
- 1102 Dai, A.: Drought under global warming: a review, *Wiley Interdisciplinary Reviews:*  
1103 *Climate Change*, 2, 45-65, 10.1002/wcc.81, 2011.
- 1104 Delany, A. C., A. C. Delany, D. W. Parkin, J. J. Griffin, E.D. Goldberg and B.E.F.  
1105 Reinmann, Airborne dust collected at Barbados, *Geochim. Cosmochim. Acta*, 885-909; 1967.
- 1106 De Souza-Machado, S., L. L. Strow, H. Motteler, and S. Hannon, Infrared dust  
1107 spectral signatures from AIRS, *Geophys. Res. Lett.*, 33, doi:10.1029/2005GL024364, 2006.
- 1108 Dolcater, D. L., J. K. Syers and M. L. Jackson, Titanium as free oxide and substituted  
1109 forms in kaolinites and other soil minerals, *Clays and Clay Minerals*, 18, 71-79, 1970.
- 1110 ECA (Economic Commission for Africa), Assessing sustainable development in  
1111 Africa. Africa's Sustainable Development Bulletin. Economic Commission for Africa, Addis  
1112 Ababa, 59 pp., 2005.
- 1113 Egan, W. G., and Hilgeman, T. W., *Optical Properties of Inhomogeneous Materials:*  
1114 *Applications to Geology, Astronomy, Chemistry, and Engineering*, Academic Press. 235 pp.  
1115 1979.
- 1116 Flamant, C., Lavaysse, C., Todd, M. C., Chaboureau, J. P., and Pelon, J.: Multi-  
1117 platform observations of a springtime case of Bodélé and Sudan dust emission, transport  
1118 and scavenging over West Africa, *Quarterly Journal of the Royal Meteorological Society*,  
1119 135, 413-430, 10.1002/qj.376, 2009.
- 1120 Formenti, P., Elbert, W., Maenhaut, W., Haywood, J., and Andreae, M. O.: Chemical  
1121 composition of mineral dust aerosol during the Saharan Dust Experiment (SHADE) airborne  
1122 campaign in the Cape Verde region, September 2000, *J. Geophys. Res.*, 108, 8576,  
1123 10.1029/2002jd002648, 2003.
- 1124 Formenti, P., Rajot, J. L., Desboeufs, K., Caquineau, S., Chevaillier, S., Nava, S.,  
1125 Gaudichet, A., Journet, E., Triquet, S., Alfaro, S., Chiari, M., Haywood, J., Coe, H., and  
1126 Highwood, E.: Regional variability of the composition of mineral dust from western Africa:  
1127 Results from the AMMA SOP0/DABEX and DODO field campaigns, *J. Geophys. Res.*, 113,  
1128 D00C13, 10.1029/2008jd009903, 2008.
- 1129 Formenti, P., Nava, S., Prati, P., Chevaillier, S., Klaver, A., Lafon, S., Mazzei, F.,  
1130 Calzolari, G., and Chiari, M.: Self-attenuation artifacts and correction factors of light element  
1131 measurements by X-ray analysis: Implication for mineral dust composition studies, *J.*  
1132 *Geophys. Res.*, 115, D01203, 10.1029/2009jd012701, 2010.



1133 Formenti, P., Schütz, L., Balkanski, Y., Desboeufs, K., Ebert, M., Kandler, K., Petzold,  
1134 A., Scheuven, D., Weinbruch, S., and Zhang, D.: Recent progress in understanding physical  
1135 and chemical properties of African and Asian mineral dust, *Atmos. Chem. Phys.*, 11, 8231-  
1136 8256, 10.5194/acp-11-8231-2011, 2011a.

1137 Formenti, P., Rajot, J. L., Desboeufs, K., Saïd, F., Grand, N., Chevaillier, S., and  
1138 Schmechtig, C.: Airborne observations of mineral dust over western Africa in the summer  
1139 Monsoon season: spatial and vertical variability of physico-chemical and optical properties,  
1140 *Atmos. Chem. Phys.*, 11, 6387-6410, 10.5194/acp-11-6387-2011, 2011b.

1141 Gillette, D., and T. R. Walker, Characteristics of airborne particles produced by wind  
1142 erosion of sandy soil, high plains of West Texas, *Soil Sci.*, 123, 97-110, 1977.

1143 Ginoux, P., J. M. Prospero, T. E. Gill, N. C. Hsu, and M. Zhao (2012), Global-scale  
1144 attribution of anthropogenic and natural dust sources and their emission rates based on  
1145 MODIS Deep Blue aerosol products, *Rev. Geophys.*, 50, RG3005,  
1146 doi:10.1029/2012RG000388.

1147 Glaccum, R. A. and J. M. Prospero, Saharan aerosols over the tropical north Atlantic -  
1148 mineralogy. *Marine Geology*, 37, 295-321, 1980.

1149 Glotch TD, Rossman GR, Aharonson O. 2007. Mid-infrared (5–100  $\mu\text{m}$ ) reflectance  
1150 spectra and optical constants of ten phyllosilicate minerals. *Icarus*. 192 : 604–622.  
1151 DOI:10.1016/j.icarus.2007.07.002.

1152 Glotch TD et Rossman GR., Mid-infrared reflectance spectra and optical constants of  
1153 six iron oxide/oxyhydroxide phases. *Icarus* 204, 663–671, 2009.

1154 Goudie, A. S., and Middleton, N. J.: Saharan dust storms: nature and consequences,  
1155 *Earth-Science Reviews* 56, 179-204, 2001.

1156 Gustafsson, R. J., A. Orlov, P. T. Griffiths, R. A. Cox, and R. M. Lambert, Reduction  
1157 of NO<sub>2</sub> to nitrous acid on illuminated titanium dioxide aerosol surfaces: implications for  
1158 photocatalysis and atmospheric chemistry, *Chem. Commun.*, 1359–7345, 3936–3938, 2006.

1159 Hansell, Jr., R. A., Reid, J. S., Tsay, S. C., Roush, T. L., and Kalashnikova, O. V., A  
1160 sensitivity study on the effects of particle chemistry, asphericity and size on the mass  
1161 extinction efficiency of mineral dust in the earth's atmosphere: from the near to thermal IR,  
1162 *Atmos. Chem. Phys.*, 11, 1527-1547, doi:10.5194/acp-11-1527-2011, 2011.

1163 Haywood, J. M., R. P. Allan, I. Culverwell, T. Slingo, S. Milton, J. Edwards, and N.  
1164 Clerbaux, Can desert dust explain the outgoing longwave radiation anomaly over the Sahara  
1165 during July 2003?, *J. Geophys. Res.*, 110, D05105, doi:10.1029/2004JD005232, 2005.

1166 Haywood, J. M., Pelon, J., Formenti, P., Bharmal, N., Brooks, M., Capes, G.,  
1167 Chazette, P., Chou, C., Christopher, S., Coe, H., Cuesta, J., Derimian, Y., Desboeufs, K.,  
1168 Greed, G., Harrison, M., Heese, B., Highwood, E. J., Johnson, B., Mallet, M., Marticorena,  
1169 B., Marsham, J., Milton, S., Myhre, G., Osborne, S. R., Parker, D. J., Rajot, J. L., Schulz, M.,  
1170 Slingo, A., Tanré, D., and Tulet, P.: Overview of the Dust and Biomass-burning Experiment  
1171 and African Monsoon Multidisciplinary Analysis Special Observing Period-0, *J. Geophys.*  
1172 *Res.*, 113, D00C17, 10.1029/2008jd010077, 2008.

1173 Haywood, J. M., Johnson, B. T., Osborne, S. R., Baran, A. J., Brooks, M., Milton, S.  
1174 F., Mulcahy, J., Walters, D., Allan, R. P., Klaver, A., Formenti, P., Brindley, H. E.,  
1175 Christopher, S., and Gupta, P.: Motivation, rationale and key results from the GERBILS  
1176 Saharan dust measurement campaign, *Quarterly Journal of the Royal Meteorological*  
1177 *Society*, 137, 1106-1116, 10.1002/qj.797, 2011.

1178 Heintzenberg, J., The SAMUM-1 experiment over Southern Morocco: overview and  
1179 introduction. *Tellus* 61B, doi:10.1111/j.1600-0889.2008.00403.x, 2008.

- 1180 Hess, M., Koepke, P., and Schult, I.: Optical properties of aerosols and clouds: The  
1181 software package OPAC, *Bull. Am. Meteorol. Soc.*, 79, 831–844, 1998.
- 1182 Highwood, E. J., J.M. Haywood, M. D. Silverstone, S.M. Newman, and J. P. Taylor,  
1183 Radiative properties and direct effect of Saharan dust measured by the C-130 aircraft during  
1184 Saharan Dust Experiment (SHADE): 2. Terrestrial spectrum, *J. Geophys. Res.*, 108(D18),  
1185 8578, doi:10.1029/2002JD002552, 2003.
- 1186 Hinds, W. C.: *Aerosol technology: properties, behavior, and measurement of airborne*  
1187 *particles*, John Wiley & Sons, Chichester, 504 pp., 1999.
- 1188 Hoose, C U Lohmann<sup>1</sup>, R Erdin<sup>1</sup> and I Tegen, The global influence of dust  
1189 mineralogical composition on heterogeneous ice nucleation in mixed-phase clouds, 2008  
1190 *Environ. Res. Lett.* 3 025003.
- 1191 Hower, J., and T. C. Mowatt, The Mineralogy of illites and mixed -layer  
1192 illite/Montmorillonites, *American Mineralogist*, 51, 825-854, 1966.
- 1193 Hudson, P. K., E. R. Gibson, M. A. Young, P. D. Kleiber, and V. H. Grassian, Coupled  
1194 infrared extinction and size distribution measurements for several clay components of  
1195 mineral dust aerosol, *J. Geophys. Res.*, 113, D01201, doi:10.1029/2007JD008791, 2008a.
- 1196 Hudson, P.K., Young, M.A., Kleiber, P.D., Grassian, V.H., coupled infrared extinction  
1197 spectra and size distribution measurements for several non-clay components of mineral dust  
1198 aerosol (quartz, calcite, and dolomite). *Atmos. Environ.* 42, 5991e5999, 2008b.
- 1199 Huneus, N., Schulz, M., Balkanski, Y., GriesFeller, J., Kinne, S., Prospero, J.,  
1200 Bauer, S., Boucher, O., Chin, M., Dentener, F., Diehl, T., Easter, R., Fillmore, D., Ghan, S.,  
1201 Ginoux, P., Grini, A., Horowitz, L., Koch, D., Krol, M. C., Landing, W., Liu, X., Mahowald, N.,  
1202 Miller, R., Morcrette, J. J., Myhre, G., Penner, J. E., Perlwitz, J., Stier, P., Takemura, T., and  
1203 Zender, C.: Global dust model intercomparison in AeroCom phase I, *Atmos. Chem. Phys.*  
1204 *Discuss.*, 10, 23781-23864, 10.5194/acpd-10-23781-2010, 2010.
- 1205 Janicot, S., Thorncroft, C. D., Ali, A., Asencio, N., Berry, G., Bock, O., Bourles, B.,  
1206 Caniaux, G., Chauvin, F., Deme, A., Kergoat, L., Lafore, J. P., Lavaysse, C., Lebel, T.,  
1207 Marticorena, B., Mounier, F., Nedelec, P., Redelsperger, J. L., Ravegnani, F., Reeves, C. E.,  
1208 Roca, R., de Rosnay, P., Schlager, H., Sultan, B., Tomasini, M., Ulanovsky, A., and team, A.  
1209 f.: Large-scale overview of the summer monsoon over West Africa during the AMMA field  
1210 experiment in 2006, *Ann. Geophys.*, 26, 2569-2595, 10.5194/angeo-26-2569-2008, 2008.
- 1211 Jickells, T. D., An, Z. S., Andersen, K. K., Baker, A. R., Bergametti, G., Brooks, N.,  
1212 Cao, J. J., Boyd, P. W., Duce, R. A., Hunter, K. A., Kawahata, H., Kubilay, N., laRoche, J.,  
1213 Liss, P. S., Mahowald, N., Prospero, J. M., Ridgwell, A. J., Tegen, I., and Torres, R.: Global  
1214 Iron Connections Between Desert Dust, Ocean Biogeochemistry, and Climate, *Science*, 308,  
1215 67-71, 10.1126/science.1105959, 2005.
- 1216 Johnson, B. T., Osborne, S. R., Haywood, J. M., and Harrison, M. A. J.: Aircraft  
1217 measurements of biomass burning aerosol over West Africa during DABEX, *J. Geophys.*  
1218 *Res.*, 113, D00C06, 10.1029/2007jd009451, 2008.
- 1219 Journet, E., Desboeufs, K. V., Caquineau, S., and Colin, J.-L.: Mineralogy as a critical  
1220 factor of dust iron solubility, *Geophys. Res. Lett.*, 35, L07805, 10.1029/2007gl031589, 2008.
- 1221 Journet, E., Balkanski, Y., and Harrison, S. P.: A new data set of soil mineralogy for  
1222 dust-cycle modeling, *Atmos. Chem. Phys.*, 14, 3801-3816, doi:10.5194/acp-14-3801-2014,  
1223 2014.
- 1224 Kandler, K., Schütz, L., Deutscher, C., Ebert, M., Hofmann, H., Jäckel, S., Jaenicke,  
1225 R., Knippertz, P., Lieke, K., Massling, A., Petzold, A., Schladitz, A., Weinzierl, B.,  
1226 Wiedensohler, A., Zorn, S., and Weinbruch, S.: Size distribution, mass concentration,  
1227 chemical and mineralogical composition and derived optical parameters of the boundary

- 1228 layer aerosol at Tinfou, Morocco, during SAMUM 2006, *Tellus B*, 61, 32-50, 10.1111/j.1600-  
1229 0889.2008.00385.x, 2009.
- 1230 Karickhoff, S. W., and Bailey, G. W.: Optical absorption spectra of clay minerals,  
1231 *Clays Clay Min.*, 21, 59-70, 1973.
- 1232 Kiefert, L., G. H. McTainsh, and W. G. Nickling, Sedimentological characteristics of  
1233 Saharan and Australian dust, in *The Impact of Desert Dust Across the Mediterranean*, edited  
1234 by S. Guerzoni and R. Chester, pp.183– 190, Kluwer Acad., Norwell, Mass., 1996.
- 1235 Klaver, A., Formenti, P., Caquineau, S., Chevaillier, S., Ausset, P., Calzolari, G.,  
1236 Osborne, S., Johnson, B., Harrison, M., and Dubovik, O.: Physico-chemical and optical  
1237 properties of Sahelian and Saharan mineral dust: in situ measurements during the GERBILS  
1238 campaign, *Quarterly Journal of the Royal Meteorological Society*, 137, 1193-1210,  
1239 10.1002/qj.889, 2011.
- 1240 Klaver, A., Estimation des propriétés optiques des poussières désertiques d'origines  
1241 saharienne et sahélienne, à proximité de leurs zones sources d'émission, à partir de leurs  
1242 propriétés physico-chimiques, thèse de Doctorat, Université Paris VII, 2012.
- 1243 Kluser, L. and Schepanski, K.: Remote sensing of mineral dust over land with MSG  
1244 infrared channels: a new Bitemporal Mineral Dust Index, *Remote Sens. Environ.*, 113, 1853–  
1245 1867, 2009
- 1246 Klüser, L., Martynenko, D., Holzer-Popp, T., Thermal infrared remote sensing of  
1247 mineral dust over land and ocean: a spectral SVD based retrieval approach for IASI. *Atmos.*  
1248 *Meas. Tech.* 4, 757e773. doi:10.5194/amt-4-757-2011, 2011.
- 1249 Klüser, L.; Kleiber, P.; Holzer-Popp, T.; Grassian, V. H., Desert Dust Observation  
1250 From Space – Application of Measured Mineral Component Infrared Extinction Spectra,  
1251 *Atmos. Environ.*, 54, 419-427, 2012.
- 1252 Köster, H. M., Ehrlicher, U., Gilg, H. A., Jordan, R., Murad, E., and Onnich, K.:  
1253 Mineralogical and chemical characteristics of five nontronites and Fe-rich smectites, *Clay*  
1254 *Minerals*, 34, 579-599, 1999.
- 1255 Koren, I., Y. J. Kaufman, R. Washington, M. C. Todd, Y. Rudich, J. Vanderlei Martins  
1256 and D. Rosenfeld, The Bodélé depression: a single spot in the Sahara that provides most of  
1257 the mineral dust to the Amazon forest, *Environ. Res. Lett.*, 1, 014005, doi:10.1088/1748-  
1258 9326/1/1/014005, 2006.
- 1259 Lafon, S., Rajot, J., Alfaro, S., and Gaudichet, A.: Quantification of iron oxides in  
1260 desert aerosol., *Atmospheric Environment*, 38, 1211-1218, 2004.
- 1261 Lafon, S., Sokolik, I. N., Rajot, J. L., Caquineau, S., and Gaudichet, A.:  
1262 Characterization of iron oxides in mineral dust aerosols: Implications for light absorption, *J.*  
1263 *Geophys. Res.*, 111, D21207, 10.1029/2005jd007016, 2006.
- 1264 Laskina, O., M. A. Young, P. D. Kleiber, and V. H. Grassian (2012), Infrared extinction  
1265 spectra of mineral dust aerosol: Single components and complex mixtures, *J. Geophys.*  
1266 *Res.*, 117, D18210, doi:10.1029/2012JD017756.
- 1267 Laurent, B., Marticorena, B., Bergametti, G., Léon, J. F., and Mahowald, N. M.:  
1268 Modeling mineral dust emissions from the Sahara desert using new surface properties and  
1269 soil database, *J. Geophys. Res.*, 113, D14218, 10.1029/2007jd009484, 2008.
- 1270 Lazaro, F. J., Gutiérrez, L., Barrón, V., and Gelado, M. D.: The speciation of iron in  
1271 desert dust collected in Gran Canaria (Canary Islands): Combined chemical, magnetic and  
1272 optical analysis, *Atmospheric Environment*, 42, 8987-8996, 2008.
- 1273 Lebel, T., Parker, D. J., Flamant, C., Bourlès, B., Marticorena, B., Mougín, E.,  
1274 Peugeot, C., Diedhiou, A., Haywood, J. M., Ngamini, J. B., Polcher, J., Redelsperger, J. L.,  
1275 and Thorncroft, C. D.: The AMMA field campaigns: multiscale and multidisciplinary

- 1276 observations in the West African region, *Quarterly Journal of the Royal Meteorological*  
1277 *Society*, 136, 8-33, 10.1002/qj.486, 2010.
- 1278 Legrand, M., N'doumé, C., and Jankowiak, I.: Satellite-derived climatology of the  
1279 Saharan aerosol., in: *Passive Infrared Remote Sensing of Clouds and the Atmosphere II*,  
1280 edited by: Lynch, D. K., SPIE, 127-135, 1994.
- 1281 Lepple, F. K., and C. J. Brine, Organic constituents in eolian dust and surface  
1282 sediments from northwest Africa, *J. Geophys. Res.*, 81, 1141–1147, 1976.
- 1283 Long LL, Querry MR, Bell RJ, Alexander RW. 1993. Optical properties of calcite and  
1284 gypsum in crystalline and powdered form in the infrared and far-infrared. *Infrared Physics*. 34  
1285 : 191-201.
- 1286 Longtin DR, Shettle EP, Hummel JR, Pryce JD. 1988. A Wind Dependent Desert  
1287 Aerosol Model: Radiative Properties. AFGL-TR-88-0112, Air Force Geophysics Laboratory,  
1288 Hanscom AFB, MA.
- 1289 Mahowald, N., Aerosol indirect effects on biogeochemistry and climate, *Science*, 334,  
1290 794, doi:10.1126/science.1207374, 2011.
- 1291 Marra AC, Blanco A, Fonti S, Jurewicz A, Orofino V. 2005. Fine hematite particles of  
1292 Martian interest: absorption spectra and optical constants. *Journal of Physics: Conference*  
1293 *Series* 6 132–138.
- 1294 Marticorena, B., and Bergametti, G.: Modeling the atmospheric dust cycle: 1. Design  
1295 of a soil-derived dust emission scheme, *J. Geophys. Res.*, 100, 16415-16430,  
1296 10.1029/95jd00690, 1995.
- 1297 Marticorena, B., Chatenet, B., Rajot, J. L., Traoré, S., Coulibaly, M., Diallo, A., Koné,  
1298 I., Maman, A., Ndiaye, T., and Zakou, A.: Temporal variability of mineral dust concentrations  
1299 over West Africa: analyses of a pluriannual monitoring from the AMMA Sahelian Dust  
1300 Transect, *Atmos. Chem. Phys.*, 10, 8899-8915, 10.5194/acp-10-8899-2010, 2010.
- 1301 Mason, B.: *Principles of Geochemistry*, 3rd ed. ed., John Wiley, New York, 1966.
- 1302 Majestic, B. J., Schauer, J. J., and Shafer, M. M.: Application of synchrotron radiation  
1303 for measurement of iron red-ox speciation in atmospherically processed aerosols, *Atmos.*  
1304 *Chem. Phys.*, 7, 2475-2487, doi:10.5194/acp-7-2475-2007, 2007.
- 1305 McConnell, C. L., Highwood, E. J., Coe, H., Formenti, P., Anderson, B., Osborne, S.,  
1306 Nava, S., Desboeufs, K., Chen, G., and Harrison, M. A. J.: Seasonal variations of the  
1307 physical and optical characteristics of Saharan dust: Results from the Dust Outflow and  
1308 Deposition to the Ocean (DODO) experiment, *J. Geophys. Res.*, 113, D14S05,  
1309 10.1029/2007jd009606, 2008.
- 1310 McConnell, C. L., Formenti, P., Highwood, E. J., and Harrison, M. A. J.: Using aircraft  
1311 measurements to determine the refractive index of Saharan dust during the DODO  
1312 Experiments, *Atmos. Chem. Phys.*, 10, 3081-3098, 10.5194/acp-10-3081-2010, 2010.
- 1313 Mehra, O. P., and Jackson, M. L.: Iron oxide removal from soils and clays by a  
1314 dithionite-citrate buffered with sodium bicarbonate, *Clay Minerals*, 7, 317-327, 1960.
- 1315 Mestdagh, M. M., L. Vielvoye and A.J. Herbillon, Iron in Kaolinite: The relationship  
1316 between kaolinite crystallinity and iron content, *Clay Minerals*, 15, 1-13, 1980.
- 1317 Mogili, P. K., Yang, K. H., Young, M. A., Kleiber, P. D., and Grassian, V. H.:  
1318 Environmental aerosol chamber studies of extinction spectra of mineral dust aerosol  
1319 components: Broadband IR-UV extinction spectra, *Journal of Geophysical Research:*  
1320 *Atmospheres*, 112, D21204, 10.1029/2007jd008890, 2007.
- 1321 Mogili, P. K., Yang, K. H., Young, M. A., Kleiber, P. D., and Grassian, V. H.: Extinction  
1322 spectra of mineral dust aerosol components in an environmental aerosol chamber: IR

- 1323 resonance studies, *Atmospheric Environment*, 42, 1752-1761,  
1324 <http://dx.doi.org/10.1016/j.atmosenv.2007.11.026>, 2008.
- 1325 Mooney, T., and R. F. Knacke, Optical Constants of Chlorite and Serpentine between  
1326 2.5 and 50  $\mu\text{m}$ , *ICARUS*, 64, 493-502, 1985.
- 1327 Müller, T., Schladitz, A., Massling, A., Kaaden, N., Kandler, K., and Wiedensohler, A.:  
1328 Spectral absorption coefficients and imaginary parts of refractive indices of Saharan dust  
1329 during SAMUM-1, *Tellus B*, 61, 79-95, 10.1111/j.1600-0889.2008.00399.x, 2009.
- 1330 Murad, E. and Wagner, U., The Mossbauer spectrum of illite, *Clay Minerals*, 29, 1-10,  
1331 1994.
- 1332 Ndour, M., B. D'Anna, C. George, O. Ka, Y. Balkanski, J. Kleffmann, K. Stemmler,  
1333 and M. Ammann, Photoenhanced uptake of  $\text{NO}_2$  on mineral dust: Laboratory experiments  
1334 and model simulations, *Geophys. Res. Lett.*, 35, doi:10.1029/2007GL032006., 2008.
- 1335 Nickovic, S., Vukovic, A., Vujadinovic, M., Djurdjevic, V., and Pejanovic, G., Technical  
1336 Note: High-resolution mineralogical database of dust-productive soils for atmospheric dust  
1337 modeling, *Atmos. Chem. Phys.*, 12, 845-855, doi:10.5194/acp-12-845-2012, 2012.
- 1338 N'Tchayi, G. M., Bertrand, J., Legrand, M., and Baudet, J.: Temporal and spatial  
1339 variations of the atmospheric dust loading throughout West Africa over the last thirty years,  
1340 *Ann. Geophys.*, 12, 265-273, doi:10.1007/s00585-994-0265-3, 1994.
- 1341 N'Tchayi Mbourou, G., Bertrand, J., and Nicholson, S. E.: The diurnal and seasonal  
1342 cycles of wind-borne dust over Africa north of the equator, *J. Appl. Meteor.*, 36, 868-882,  
1343 1997.
- 1344 O'Day, P. A., Rivera, N., Root, R., and Carroll, S. A.: X-ray absorption spectroscopic  
1345 study of Fe reference compounds for the analysis of natural sediments, *American  
1346 Mineralogist*, 89, 572-585, 2004.
- 1347 Ohta, A., Tsuno, H., Kagi, H., Kanai, Y., Nomura, M., Zhang, R., Terashima, N., and  
1348 Imai, N.: Chemical compositions and XANES speciations of Fe, Mn and Zn from aerosols  
1349 collected in China and Japan during dust events, *Geochemical Journal*, 40, 363-376, 2006.
- 1350 Paquet, H., Coudé-Gaussen, G., and Rognon, P.: Etude minéralogique de poussières  
1351 sahariennes le long d'un itinéraire entre 19° et 35° de latitude nord, *Révue de Géologie  
1352 Dynamique et de Géographie Physique*, 25, 257-265, 1984.
- 1353 Paris, R., Desboeufs, K. V., and Journet, E.: Variability of dust iron solubility in  
1354 atmospheric waters: Investigation of the role of oxalate organic complexation, *Atmospheric  
1355 Environment*, 45, 6510-6517, <http://dx.doi.org/10.1016/j.atmosenv.2011.08.068>, 2011.
- 1356 Patterson, E., Gillette, D., and Stockton, B.: Complex index of refraction between 300  
1357 and 700 nm for Saharan aerosols, *J. Geophys. Res.*, 82, 3153-3160, 1977.
- 1358 Pentrakova, L., SU, K., Pentak, M., and J. W. Stucki, A review of microbial redox  
1359 interactions with structural Fe in clay minerals, *Clay Minerals*, 48, 543-560, 2013.
- 1360 Peterson JT et Weinman JA. 1969. Optical properties of quartz dust particles at  
1361 infrared wavelengths. *Journal of Geophysical Research Letters*. 74 : 6947-6952.
- 1362 Prietzel, J., Thieme, J., Eusterhues, K., and Eichert, D.: Iron speciation in soils and  
1363 soil aggregates by synchrotron-based x. ray microspectroscopy (xanes, mu-xanes), *Eur. J.  
1364 Soil. Sci.*, 58, 1027-1041, 2007.
- 1365 Prospero, J. M., Ginoux, P., Torres, O., Nicholson, S. E., and Gill, T. E.:  
1366 Environmental characterization of global sources of atmospheric soil dust identified with the  
1367 Nimbus 7 Total Ozone Mapping Spectrometer (TOMS) absorbing aerosol product., *Rev.  
1368 Geophys.*, 40, 2-1 to 2-31, 2002.
- 1369 Pye, K.: *Aeolian Dust and Dust Deposits*, Academic Press, London, 334 pp., 1987.

- 1370 Query MR, Osborne G, Lies K, Jordon R, Coveney RM. 1978. Complex refractive  
1371 index of limestone in the visible and infrared. *Applied Optics*. 17 : 353–356.
- 1372 Query MR. 1987. Optical constants of minerals and other materials from the  
1373 millimeter to the UV. U.S. Army Rep. CRDEC-CR- 88009, Aberdeen, MD.
- 1374 Rahn, K. A.: Silicon and aluminum in atmospheric aerosols: crust-air fractionation?,  
1375 *Atmos. Environ.*, 10, 597-601, 1976.
- 1376 Rajot, J.-L.: Wind blown sediment mass budget of Sahelian village land units in  
1377 Niger., *Bull. Soc. Géol. France*, 172, 523-531, 2001.
- 1378 Rajot, J. L., Formenti, P., Alfaro, S., Desboeufs, K., Chevaillier, S., Chatenet, B.,  
1379 Gaudichet, A., Journet, E., Marticorena, B., Triquet, S., Maman, A., Mouget, N., and Zakou,  
1380 A.: AMMA dust experiment: An overview of measurements performed during the dry season  
1381 special observation period (SOP0) at the Banizoumbou (Niger) supersite, *J. Geophys. Res.*,  
1382 113, D00C14, 10.1029/2008jd009906, 2008.
- 1383 Redelsperger, J.-L., Thorncroft, C. D., Diedhiou, A., Lebel, T., Parker, D. J., and  
1384 Polcher, J.: African Monsoon Multidisciplinary Analysis: An International Research Project  
1385 and Field Campaign, *Bulletin of the American Meteorological Society*, 87, 1739-1746,  
1386 doi:10.1175/BAMS-87-12-1739, 2006.
- 1387 Reeves, C. E., Formenti, P., Afif, C., Ancellet, G., Attié, J. L., Bechara, J., Borbon, A.,  
1388 Cairo, F., Coe, H., Crumeyrolle, S., Fierli, F., Flamant, C., Gomes, L., Hamburger, T.,  
1389 Jambert, C., Law, K. S., Mari, C., Jones, R. L., Matsuki, A., Mead, M. I., Methven, J., Mills, G.  
1390 P., Minikin, A., Murphy, J. G., Nielsen, J. K., Oram, D. E., Parker, D. J., Richter, A., Schlager,  
1391 H., Schwarzenboeck, A., and Thouret, V.: Chemical and aerosol characterisation of the  
1392 troposphere over West Africa during the monsoon period as part of AMMA, *Atmos. Chem.*  
1393 *Phys.*, 10, 7575-7601, 10.5194/acp-10-7575-2010, 2010.
- 1394 Reid, E. A., Reid, J. S., Meier, M. M., Dunlap, M. R., Cliff, S. S., Broumas, A., Perry,  
1395 K., and Maring, H.: Characterization of African dust transported to Puerto Rico by individual  
1396 particle and size segregated bulk analysis, *J. Geophys. Res.*, 108, 8591,  
1397 10.1029/2002jd002935, 2003.
- 1398 Saïd, F., Canut, G., Durand, P., Lohou, F., and Lothon, M.: Seasonal evolution of  
1399 boundary-layer turbulence measured by aircraft during the AMMA 2006 Special Observation  
1400 Period, *Quarterly Journal of the Royal Meteorological Society*, 136, 47-65, 10.1002/qj.475,  
1401 2010.
- 1402 Schepanski, K., I. Tegen, B. Laurent, B. Heinold, and A. Macke, A new Saharan dust  
1403 source activation frequency map derived from MSG-SEVIRI IR channels, *Geophys. Res.*  
1404 *Lett.*, 34, L18803, doi:10.1029/ 2007GL030168, 2007.
- 1405 Schepanski, K., Tegen, I., Todd, M. C., Heinold, B., Bönisch, G., Laurent, B., and  
1406 Macke, A.: Meteorological processes forcing Saharan dust emission inferred from MSG-  
1407 SEVIRI observations of subdaily dust source activation and numerical models, *J. Geophys.*  
1408 *Res.*, 114, D10201, 10.1029/2008jd010325, 2009.
- 1409 Schepanski, K., I. Tegen, A. Macke, Comparison of satellite based observations of  
1410 Saharan dust source areas, *Remote Sensing of Environment*, 123, 90–97, 2012.
- 1411 Scheuvs, D., Schütz, L., Kandler, K., Ebert, M., and (2007), Weinbruch, S.: Bulk  
1412 composition of northern African dust and its source sediments — A compilation, *Earth-*  
1413 *Science Reviews*, 116, 170-194, <http://dx.doi.org/10.1016/j.earscirev.2012.08.005>, 2013.
- 1414 Smith A. J. A. and Grainger, R. G., Does variation in mineral composition alter the  
1415 short-wave light scattering properties of desert dust aerosol? *J. Quant. Spectrosc. Radiat.*  
1416 *Transfer*, <http://dx.doi.org/10.1016/j.jqsrt.2013.08.005i>, 2013.

1417 Schroth, A. W., Crusius, J., Sholkovitz, E. R., and Bostick, B. C.: Iron solubility driven  
1418 by speciation in dust sources to the ocean, *Nature Geosci.*, 2, 337-340, 2009.

1419 Shao, Y., Wyrwoll, K.-H., Chappell, A., Huang, J., Lin, Z., McTainsh, G. H., Mikami,  
1420 M., Tanaka, T. Y., Wang, X., and Yoon, S.: Dust cycle: An emerging core theme in Earth  
1421 system science, *Aeolian Research*, 2, 181-204,  
1422 <http://dx.doi.org/10.1016/j.aeolia.2011.02.001>, 2011.

1423 Shettle, E. P. and Fenn, R. W., *Models for the Aerosols of the Lower Atmosphere and*  
1424 *the Effects of Humidity Variations on Their Optical Properties.* AFGL-TR-79-0214,  
1425 ADA085951, 1979.

1426 Shi, Z., et al. (2011), Influence of chemical weathering and aging of iron oxides on the  
1427 potential iron solubility of Saharan dust during simulated atmospheric processing, *Global*  
1428 *Biogeochem. Cycles*, 25, GB2010, doi:10.1029/2010GB003837.

1429 Shi, Z., Michael D. Krom, Timothy D. Jickells, Steeve Bonneville, Kenneth S. Carslaw,  
1430 Nikos Mihalopoulos, Alex R. Baker, Liane G. Benning, Impacts on iron solubility in the  
1431 mineral dust by processes in the source region and the atmosphere: A review, *Aeolian*  
1432 *Research*, Volume 5, August 2012, Pages 21-42

1433 Sokolik, I. N., Toon, O. B., Bergstrom, R. W., Modeling the radiative characteristics of  
1434 airborne mineral aerosols at infrared wavelengths. *Journal of Geophysical Research Letters*.  
1435 103 : 8813-8826, 1998.

1436 Sokolik, I., and Toon, O.: Incorporation of mineralogical composition into models of  
1437 the radiative properties of mineral aerosol from UV to IR wavelengths, *J. Geophys. Res.*,  
1438 104, 9423-9444, 1999.

1439 Sokolik, I. N., Winker, D. M., Bergametti, G., Gillette, D. A., Carmichael, G., Kaufman,  
1440 Y. J., Gomes, L., Schuetz, L., and Penner, J. E.: Introduction to special section: Outstanding  
1441 problems in quantifying the radiative impacts of mineral dust, *J. Geophys. Res.*, 106, 18015-  
1442 18027, 10.1029/2000jd900498, 2001.

1443 Sow, M., Alfaro, S. C., Rajot, J. L., and Marticorena, B.: Size resolved dust emission  
1444 fluxes measured in Niger during 3 dust storms of the AMMA experiment, *Atmos. Chem.*  
1445 *Phys.*, 9, 3881-3891, 10.5194/acp-9-3881-2009, 2009.

1446 Spitzer WG et Kleinman DA. 1961. Infrared lattice bands of quartz. *Physical Review*.  
1447 121 : 1324-1335.

1448 Tegen, I., and Fung, I.: Modeling of mineral dust in the atmosphere: Sources,  
1449 transport, and optical thickness., *J. Geophys. Res.*, 99, 22897-22914, 1994.

1450 Toon, O. B., Pollock, J. B., Khare, B. N., The optical constants of several atmospheric  
1451 aerosols species: ammonium sulfate, aluminum oxide and sodium chloride, *Journal of*  
1452 *Geophysical Research Letters*. 81, 5733-5748, 1976.

1453 Tulet, P., Mallet, M., Pont, V., Pelon, J. and Boone, A., The 7-13 March 2006 dust  
1454 storm over West Africa: Generation, transport, and vertical stratification, *J. Geophys. Res.*,  
1455 113, doi: 10.1029/2008JD009871, 2008.

1456 Washington, R., Todd, M., Middleton, N. J., and Goudie, A. S., Dust-storm source  
1457 areas determined by the total ozone monitoring spectrometer and surface observations.  
1458 *Annals of the Association of American Geographers*, 93(2), 297–313, 2003.

1459 Washington, R., Todd, M. C., Engelstaedter, S., Mbainayel, S., and Mitchell, F.: Dust  
1460 and the low-level circulation over the Bodélé Depression, Chad: Observations from BoDEx  
1461 2005, *J. Geophys. Res.*, 111, D03201, 10.1029/2005jd006502, 2006.

1462 Washington, R., Flamant, C., Parker, D. J., Marsham, J., McQuaid, J. B., Brindley, H.,  
1463 Todd, M., Highwood, E. J., Chaboureau, J.-P., Kocha, C., Bechir, M., Saci, A., and Ryder, C.  
1464 L.: Fennec – The Saharan Climate System, submitted to CLIVAR Exchanges, 2013.

- 1465           Wilke, M., Farges, F., Petit, P.-E., Brown, G. E. J., and Mertin, F.: Oxidation state and  
1466 coordination of Fe in minerals: An Fe K-XANES spectroscopic study, *American Mineralogist*,  
1467 86, 714-730, 2001.
- 1468           Yoshioka, M., Mahowald, N., Dufresne, J.-L., and Luo, C.: Simulation of absorbing  
1469 aerosol indices for African dust, *J. Geophys. Res.*, 110, D18S17, 10.1029/2004jd005276,  
1470 2005.
- 1471



## 1472 **Table captions**

1473 Table 1. Calibration coefficients by mineral obtained for the calibration of the XRD analyser  
1474 used in this study. The calibration coefficients represent the slope of the correlation line  
1475 between the number of diffracted counts by unit mass. The references of the standard  
1476 minerals used in this study are also reported.

1477 Table 2. Mean values of the relative proportions of iron in the form of hematite and goethite  
1478 to total iron oxide as obtained by XAS/XANES analysis. Standard deviations are indicated in  
1479 parenthesis.

1480 Table 3. Mineralogical composition (percentage by mass, in %) according to the source  
1481 region. Standard deviations are indicated in parenthesis.

1482 Table 4. Complex refractive indices of individual minerals used in this study. The spectral  
1483 domains are indicated. \*Longtin et al. (1988) have compiled values of complex refractive  
1484 indices for hematite and quartz based on different sources.

## 1485 **Figure captions**

1486 Figure 1. Comparison between the total estimated dust mass (TEDM) estimated from the  
1487 chemical composition and the total dry gravimetric mass (TDGM) for the AMMA SOP0 (open  
1488 circles) and AMMA SOP1-2 data (black circles). The dashed line represents the slope of the  
1489 calculated linear regression.

1490 Figure 2. Geographical identification of the origin of the analysed samples superimposed to  
1491 the localisation of the major potential source areas (PSA) of mineral dust in western and  
1492 northern Africa proposed by Formenti et al. (2011a) and Scheuvens et al. (2013) on the basis  
1493 of the analysis of satellite products and chemical/mineralogical composition on the aerosol  
1494 and the parent soil. The approximate localisation of the Sahelian dust sources is also  
1495 indicated by the shed grey area. The location of the Banizoumbou ground-based site is  
1496 indicated by the black cross. The operating areas of the AMMA, DABEX, DODO and  
1497 GERBILS field projects are shown. Figure reproduced from Scheuvens et al. (2013) with  
1498 permission from Elsevier.

1499 Figure 3. Scatterplot of the elemental ratio Fe/Ca versus Si/Al with additional information on  
1500 source identification based on back-trajectory/satellite and dispersion modeling.

1501 Figure 4. Range of variability of the mineral content (in percent) as obtained by XRD  
1502 analysis. Boxes indicate the 25, 50 and 75% percentiles. Whiskers indicate the minimum and  
1503 the maximum values, whereas the open squares indicate the mean value of the distribution.

1504 Figure 5. Variability of the iron oxide content (ratio of Fe<sub>ox</sub> to total elemental Fe) according to  
1505 the source region. Boxes indicate the 25, 50 and 75% percentiles. Whiskers indicate the  
1506 minimum and the maximum values, and points indicate the 5 and 95% percentiles. Data  
1507 labels are as follows: Mo = Morocco; Ma = Mali; Mau = Mauritania; SA = South Algeria; NN =  
1508 North Niger. Figure 6. Dependence of the Fe<sub>ox</sub> content (Fe<sub>ox-to-Fe</sub> ratio) on the Fe/Ca ratio  
1509 for samples of different source regions identified in this work.

1510 Figure 7. Scatterplot of the estimated mass of TiO<sub>2</sub> with respect to the total dust mass (TDM).  
1511 Open circles are used to display values for samples corresponding to transport of Saharan  
1512 dust, whereas filled circles are for samples corresponding to local emission in the Sahel.

1513 Figure 8. Scatterplot of the Ti/Fe ratio with respect to the Fe<sub>ox-to-Fe</sub> ratio.

1514 Figure 9. Normalized volume size distribution dV/dlog(EOD) at Banizoumbou during three  
1515 consequent days in summer (J1 red line, J2 green line, J3 blue line) and one day in winter  
1516 (black line) for samples representing dust transported from the Bodélé source region. Data  
1517 are reported as a function of the equivalent optical diameter (EOD) as obtained by optical  
1518 counter measurements without any corrections for the sample refractive index.

1519 Figure 10. Normalised volume size distribution  $dV/d\log(EOD)$  for samples representing dust  
1520 of emitted dust in the Sahel during episodes local erosions. The explanation of the sample ID  
1521 is reported in the text.

1522 Figure 11. Imaginary part of the complex refractive index calculated from the mineralogical  
1523 composition of dust originating from sources PSA5, PSA4, PSA3, local erosion in the Sahel,  
1524 and PSA2 (from top to bottom). Figure 11.a represents the real part in the 0.3-0.7  $\mu\text{m}$ ,  
1525 calculated assuming refractive index from Table 3. Grey shaded curves represent results  
1526 obtained when using the data from Bedidi and Cervelle (1993) for hematite, whereas blue  
1527 shaded areas correspond to using values from Shettle (1979). Figure 11.b represents the  
1528 imaginary part of the complex refractive index calculated in the 6-16  $\mu\text{m}$  spectral domain.  
1529 The black line with white diamonds represents data from the OPAC database (Hess et al.,  
1530 1998).

1531 Figure 12. Iron solubility calculated from the mineralogical composition and from CBD  
1532 analysis as a function of emission source. Error bars indicate standard deviation. When error  
1533 bar is not presented, the data is only for one sample.

1534  
1535

1536 Table 1. Calibration coefficients by mineral obtained from the calibration of the XRD analyser  
 1537 used in this study. The calibration coefficients represent the slope of the linear correlation  
 1538 between the number of diffracted counts by unit mass. The references of the standard  
 1539 minerals used in this study are also reported. The absolute uncertainty on the slope is also  
 1540 indicated, whereas numbers in parenthesis are the percent uncertainty obtained as ratio  
 1541 between the absolute uncertainty and slope value.

Mineral	Origin	Slope (cps mg <sup>-1</sup> )	R <sup>2</sup>
Quartz (SiO <sub>2</sub> )	Fontainebleau, France	446 ± 14 (3%)	0.88
Calcite (CaCO <sub>3</sub> )	Bédarieux, France	325 ± 11 (3%)	0.94
Dolomite (CaMg(CO <sub>3</sub> ) <sub>2</sub> )	Traversella, Italie	679 ± 70 (10%)	0.55
Gypsum (CaSO <sub>4</sub> 2H <sub>2</sub> O)	Unknown	446 ± 22 (5%)	0.89
Ortoclase (KAlSi <sub>3</sub> O <sub>8</sub> )	Madagascar	997 ± 70 (7%)	0.69
Albite (NaAlSi <sub>3</sub> O <sub>8</sub> )	Ontario, Canada	2456 ± 56 (2%)	0.96

1542

1543

1544 Table 2. Mean percent values of the oxide fraction of total Fe and relative proportions of  
 1545 hematite and goethite to total iron oxide as obtained by XAS/XANES analysis. Standard  
 1546 deviations are indicated in parenthesis.

Origin	Oxide fraction of total Fe (%)	Goethite fraction of Fe oxide (%)	Hematite fraction of Fe oxide (%)
PSA5 (Bodélé)	43 ( $\pm$ 11)	65 ( $\pm$ 7)	35 ( $\pm$ 7)
PSA3 (North Niger)	57 ( $\pm$ 2)	59 ( $\pm$ 8)	41 ( $\pm$ 8)
PSA3 (South Algeria)	55 (---)	62 (---)	38 (---)
Erosion, Sahel	66 ( $\pm$ 5)	68 ( $\pm$ 5)	32 ( $\pm$ 5)

1547 Table 3. Mineralogical composition (percentage by mass, in %) according to the source region. Standard deviations are indicated in parenthesis.

Source	Kaolinite	Illite	Quartz	Ortoclase	Albite	Calcite	Dolomite	Gypsum	Goethite	Hematite	Titanium oxide
Bodélé (wintertime)	84.1 (--)	8.5 (--)	2.9 (--)	0.2 (--)	< DL	0.9 (--)	< DL	0.2 (--)	1.6 (--)	1.1 (--)	0.7
Bodélé/Sudan (summertime)	76.1 (4.4)	7.0 (0.4)	11.2 (5.6)	0.5 (0.2)	0.1 (0.1)	1.3 (0.8)	0.3 (0.1)	0.2 (--)	2.0 (0.3)	1.3 (0.3)	0.7
North Niger/Libya	54.0 (--)	37.8 (--)	4.6 (--)	0.2 (--)	< DL	0.4 (--)	< DL	< DL	1.5 (--)	0.8 (--)	0.8
North Niger/Libya/south Algeria	60.5 (4.7)	24.0 (1.9)	3.6 (3.1)	0.2 (--)	< DL	6.3 (2.9)	< DL	< DL	3.1 (0.2)	1.6 (0.1)	0.8
South Algeria/Mali	71.1 (13.5)	16.4 (11.8)	7.1 (0.8)	0.4 (0.2)	0.2 (0.1)	1.5 (0.01)	0.7 (0.4)	0.3 (--)	1.1 (0.1)	0.8 (0.05)	0.8
South Algeria/North Niger (smectites)	75.2 (3)	7.0 (0.3)	10.8 (2.0)	0.6 (0.2)	0.1 (0.1)	0.9 (0.6)	0.4 (0.2)	0.5 (--)	2.4 (0.6)	1.7 (0.4)	0.8
South Algeria/North Niger (non smectites)	78.2 (2.2)	7.2 (0.2)	6.6 (0.7)	0.4 (0.1)	0.1 (0.02)	3.0 (3.6)	0.2 (0.05)	0.6 (0.3)	2.4 (1.5)	1.8 (1.1)	0.8
North Niger	78.3 (--)	7.4 (--)	9.7 (--)	0.5 (--)	0.1 (--)	< DL	0.3 (--)	0.9 (--)	1.4 (--)	0.7 (--)	0.8
Local erosion (all)	73.0 (13)	7.1 (1.3)	14.3 (13)	0.8 (1)	0.1 (0.2)	< DL	0.1 (--)	0.3 (0.3)	2.1 (0.5)	1.2 (0.4)	1.3
Local erosion (quartz-rich)	46.6 (--)	4.4 (--)	40.6 (--)	2.9 (--)	0.4 (--)	< DL	< DL	< DL	2.4 (--)	1.4 (--)	1.4
Local erosion (excluding quartz-rich)	78.3 (1.5)	7.5 (0.2)	9.1 (2.2)	0.4 (0.1)	< DL	< DL	0.1 (--)	0.3 (0.3)	2.0 (0.6)	1.1 (0.4)	1.4
Mali/Mauritania	29.7 (--)	46.3 (--)	17.3 (--)	1.3 (--)	0.4 (--)	1.0 (--)	0.8 (--)	< DL	1.3 (--)	0.7 (--)x	1.3
Mali/Mauritania/Western Sahara	30.7 (3.2)	54.2 (6.0)	8.4 (1.7)	0.3 (0.1)	0.2 (0.2)	1.2 (0.9)	0.2 (0.2)	0.4 (--)	2.0 (0.5)	1.3 (0.3)	1.3

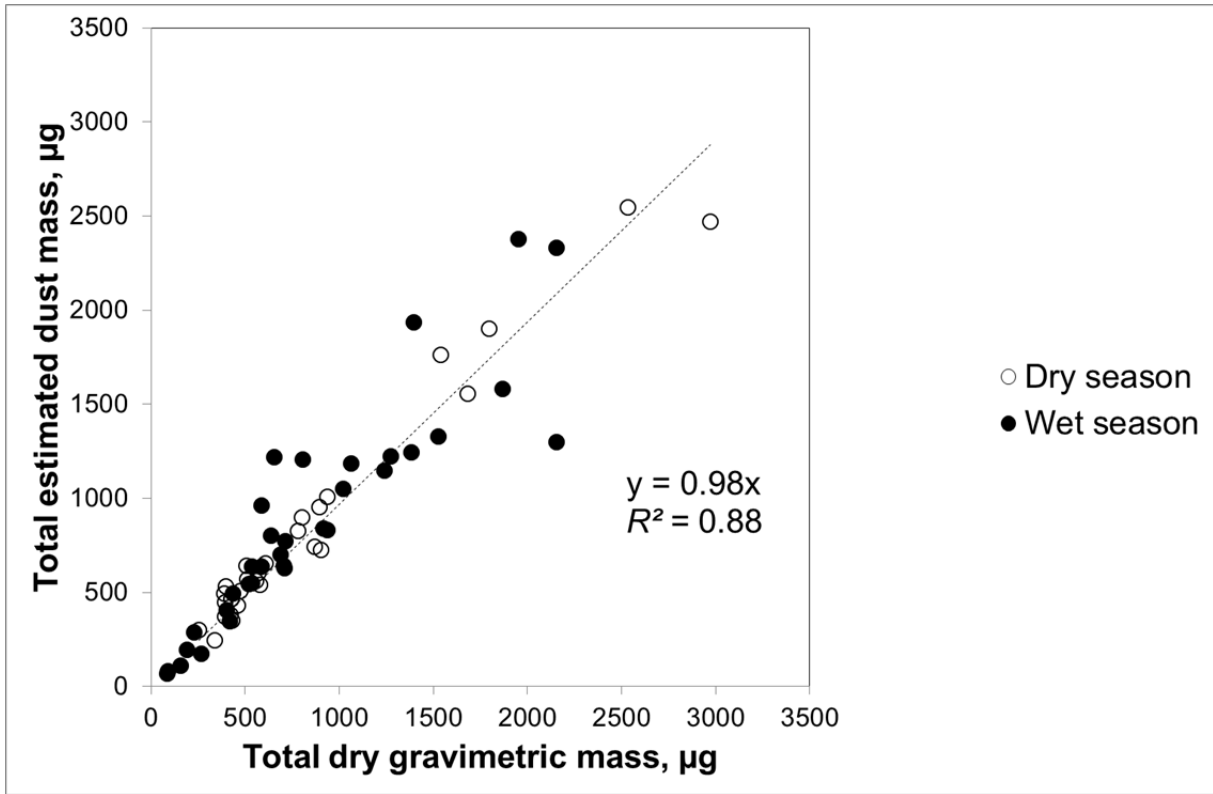
1548 Table 4. Complex refractive indices of individual minerals used in this study. The spectral  
 1549 domains are indicated. \*Longtin et al. (1988) have compiled values of complex refractive  
 1550 indices for hematite and quartz based on different sources.

<b>Mineral</b>	<b>Reference</b>	<b>Spectral domain (<math>\mu\text{m}</math>)</b>
<b>Illite</b>	Egan et Hilgeman (1979)	0.185-2.6
	Querry (1987)	2.5-200
	Glotch et al. (2007)	5-100
<b>Kaolinite</b>	Egan et Hilgeman (1979)	0.185-2.6
	Roush et al. (1991)	5-25
	Glotch et al. (2007)	5-100
<b>Calcite</b>	Querry (1978)	0.2-25
	Long et al. (1993)	2.5-300
<b>Dolomite</b>	Barthelmy (2007)	0.185-2.5
	Querry (1987)	2.5-40
<b>Albite</b>	Barthelmy (2007)	0.185-2.5
<b>Orthoclase</b>	Barthelmy (2007)	0.185-2.5
<b>Gypsum</b>	Barthelmy (2007)	0.185-2.5
	Long et al. (1993)	2.5-300
<b>Goethite</b>	Bedidi et Cervelle (1993)	0.46-0.7
	Glotch et Rossman (2009)	8.3-50
<b>Hematite</b>	Bedidi et Cervelle (1993)	0.4-0.7
	Marra et al., (2005)	6.5-50
	Longtin et al. (1988)*	0.2-300
<b>Quartz</b>	Longtin et al.,(1988)*	0.2-2
	Peterson et Weinman (1969)	5-36
	Spitzer et Kleinman (1961)	5-37

1551

1552

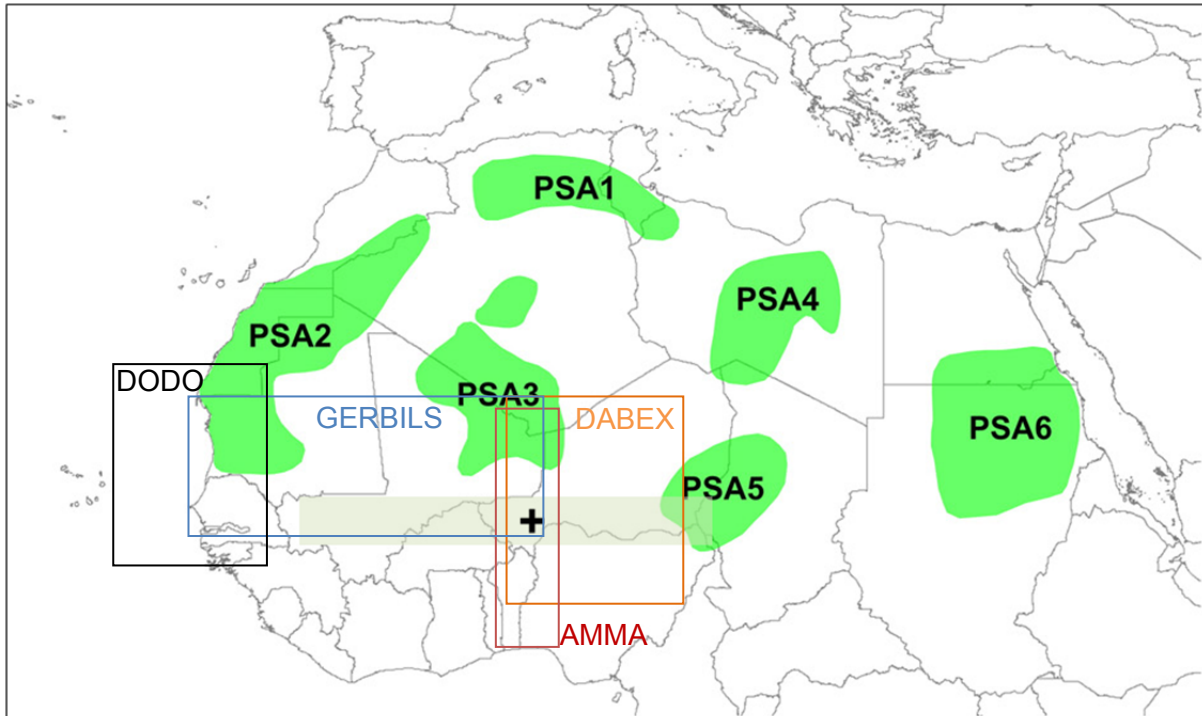
1553 Figure 1. Comparison between the total estimated dust mass (TEDM) estimated from the  
1554 chemical composition and the total dry gravimetric mass (TDGM) for the AMMA SOP0 (open  
1555 circles) and AMMA SOP1-2 data (black circles). The dashed line represents the slope of the  
1556 calculated linear regression.



1557

1558

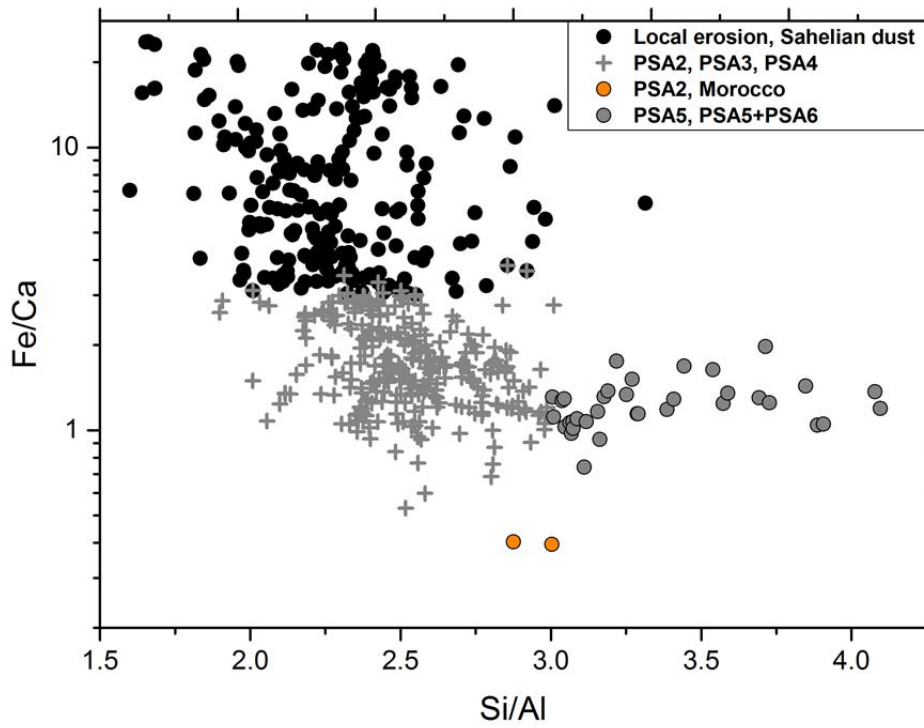
1559 Figure 2. Geographical identification of the origin of the analysed samples superimposed to  
1560 the localisation of the major potential source areas (PSA) of mineral dust in western and  
1561 northern Africa proposed by Formenti et al. (2011a) and Scheuvsens et al. (2013) on the basis  
1562 of the analysis of satellite products and chemical/mineralogical composition on the aerosol  
1563 and the parent soil (Claquin et al., 1999; Brooks and Legrand, 2000; Caquineau et al., 2002;  
1564 Prospero et al., 2002; Washington et al., 2003; Schepanski et al., 2007; 2009; 2012; Laurent  
1565 et al., 2008; Klüser and Schepanski, 2009). The approximate localisation of the Sahelian  
1566 dust sources is also indicated by the shed grey area. The location of the Banizoumbou  
1567 ground-based site is indicated by the black cross. The operating areas of the AMMA,  
1568 DABEX, DOD and GERBILS field projects are shown. Figure reproduced from Scheuvsens et  
1569 al. (2013) with permission from Elsevier.



1570  
1571  
1572

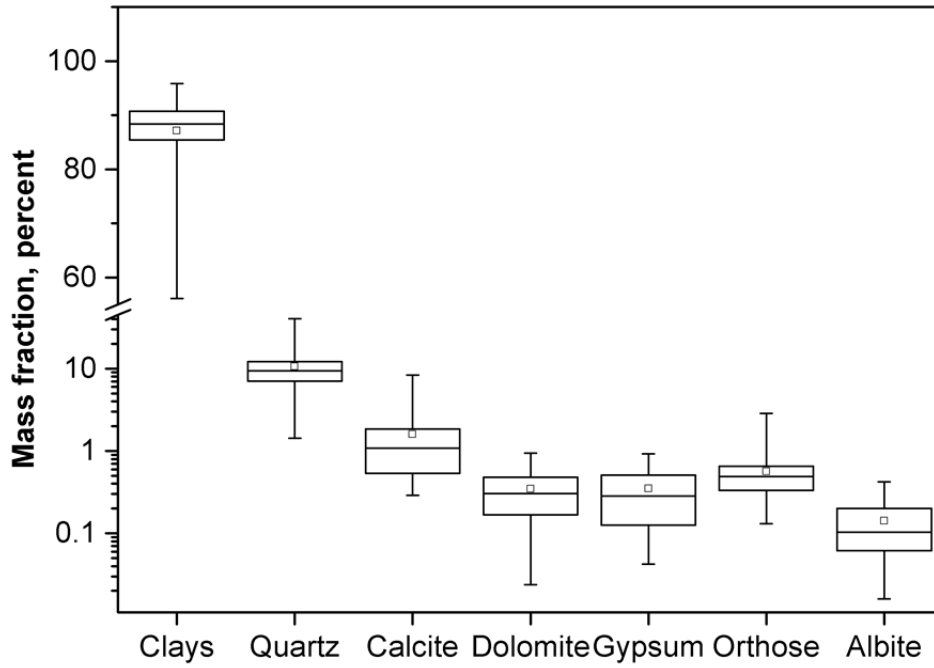


1573 Figure 3. Scatterplot of the elemental ratio Fe/Ca versus Si/Al with additional information on  
1574 source identification based on back-trajectory/satellite and dispersion modeling.



1575  
1576

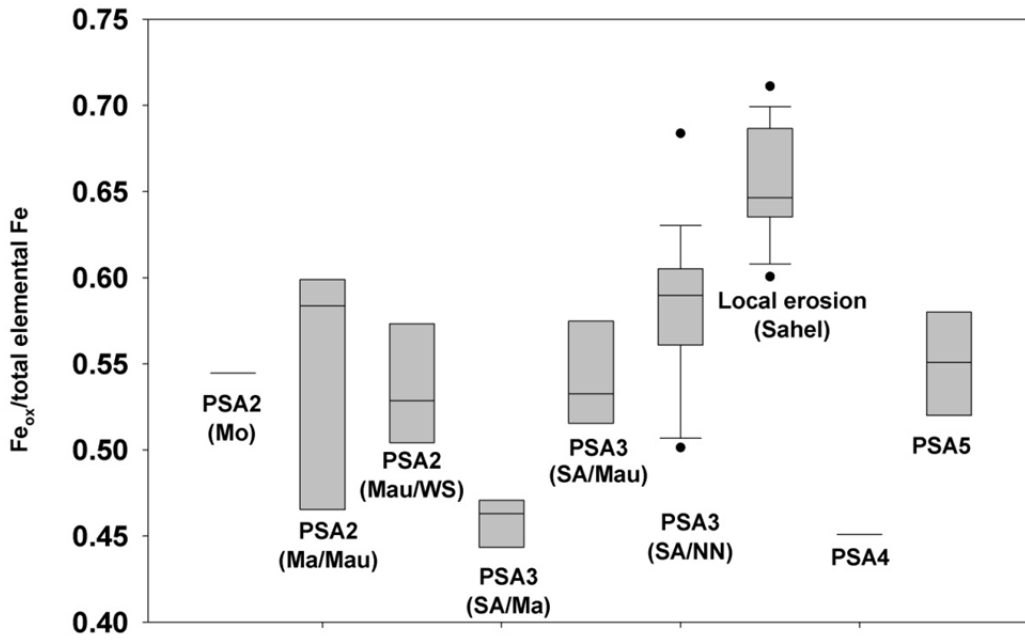
1577 Figure 4. Range of variability of the mineral mass fraction (in percent) as obtained by XRD  
1578 analysis. Boxes indicate the 25, 50 and 75% percentiles. Whiskers indicate the minimum and  
1579 the maximum values, whereas the open squares indicate the mean value of the distribution.



1580

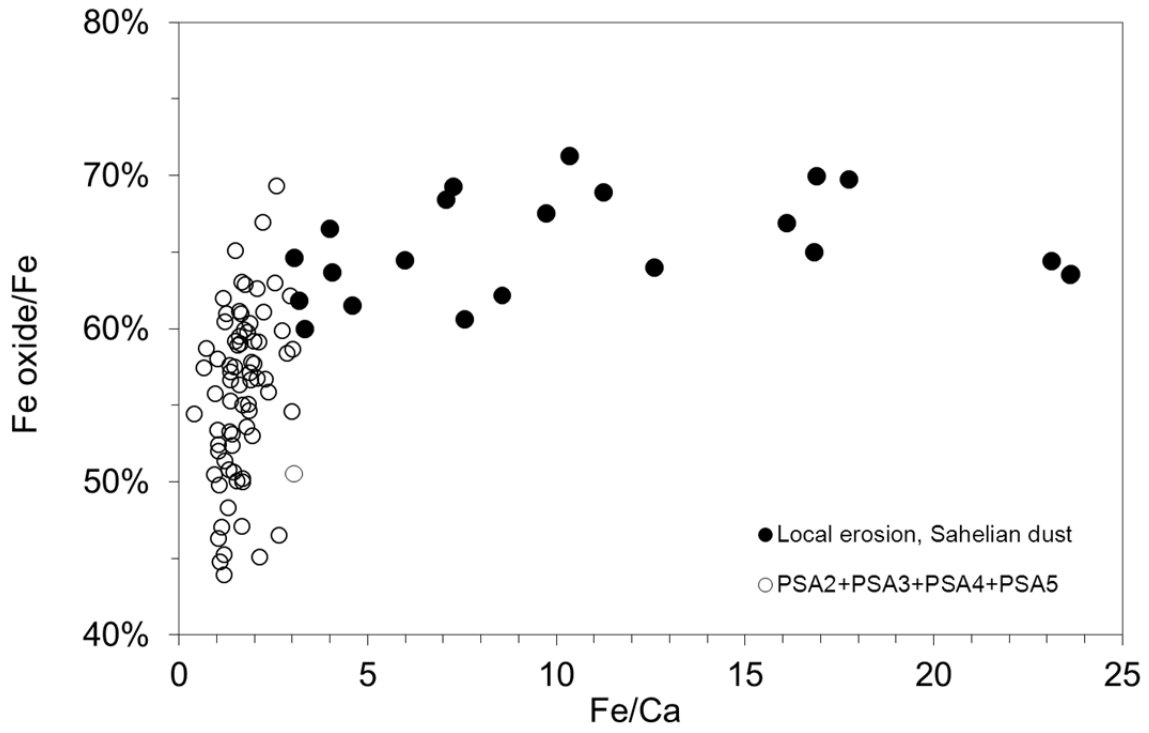
1581

1582 Figure 5. Variability of the iron oxide content (ratio of  $Fe_{ox}$  to total elemental Fe) according to  
 1583 the source region. Boxes indicate the 25, 50 and 75% percentiles. Points indicate the  
 1584 minimum and the maximum values, and Whiskers indicate the 5 and 95% percentiles. Data  
 1585 labels are as follows: Mo = Morocco; Ma = Mali; Mau = Mauritania; SA = South Algeria; NN =  
 1586 North Niger.



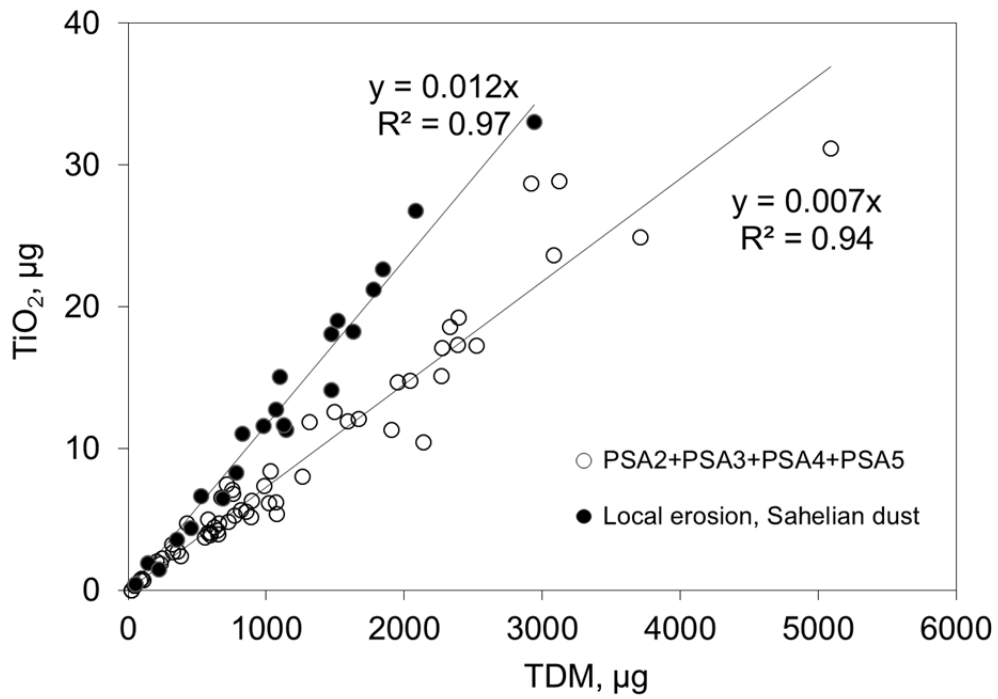
1587  
 1588

1589 Figure 6. Dependence of the  $Fe_{ox}$  content ( $Fe_{ox}$ -to- $Fe$  ratio) on the  $Fe/Ca$  ratio for samples  
1590 of different source regions identified in this work.



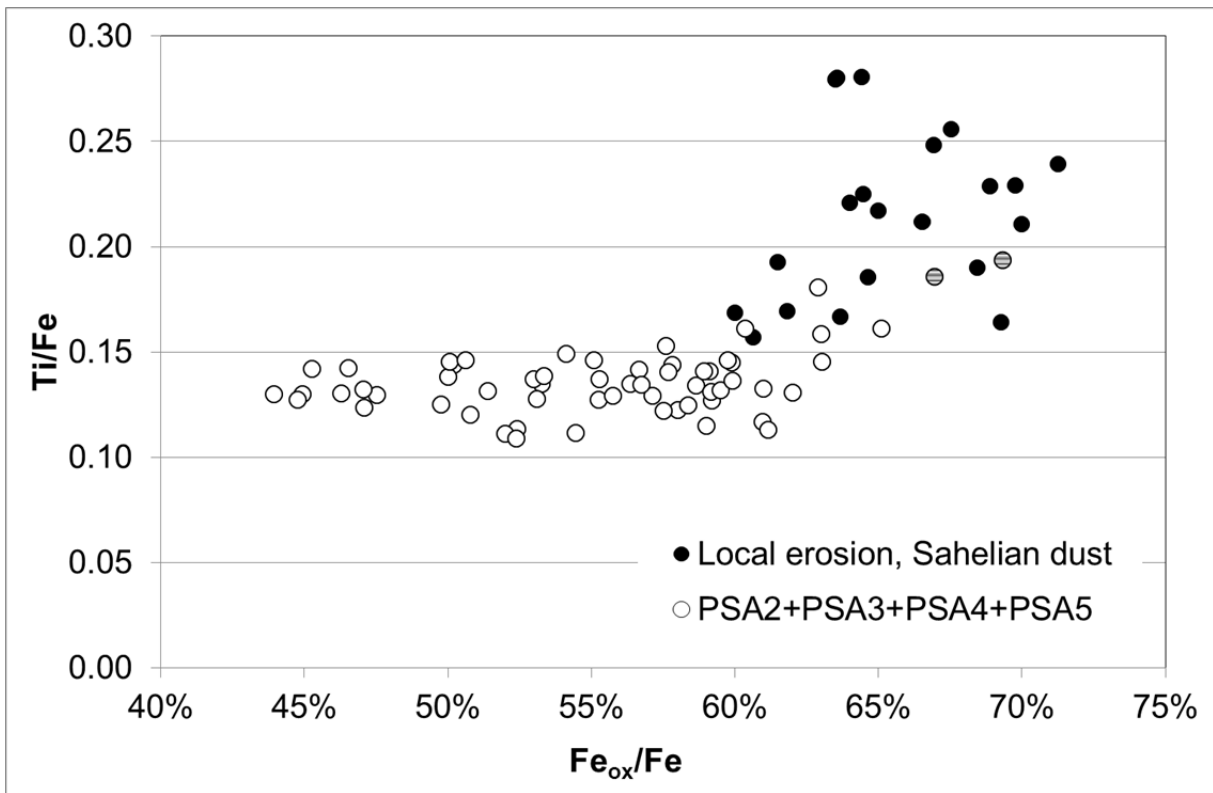
1591  
1592

1593 Figure 7. Scatterplot of the estimated mass of  $\text{TiO}_2$  with respect to the total dust mass (TDM).  
1594 Open circles are used to display values for samples corresponding to transport of Saharan  
1595 dust, whereas filled circles are for samples corresponding to local emission in the Sahel.



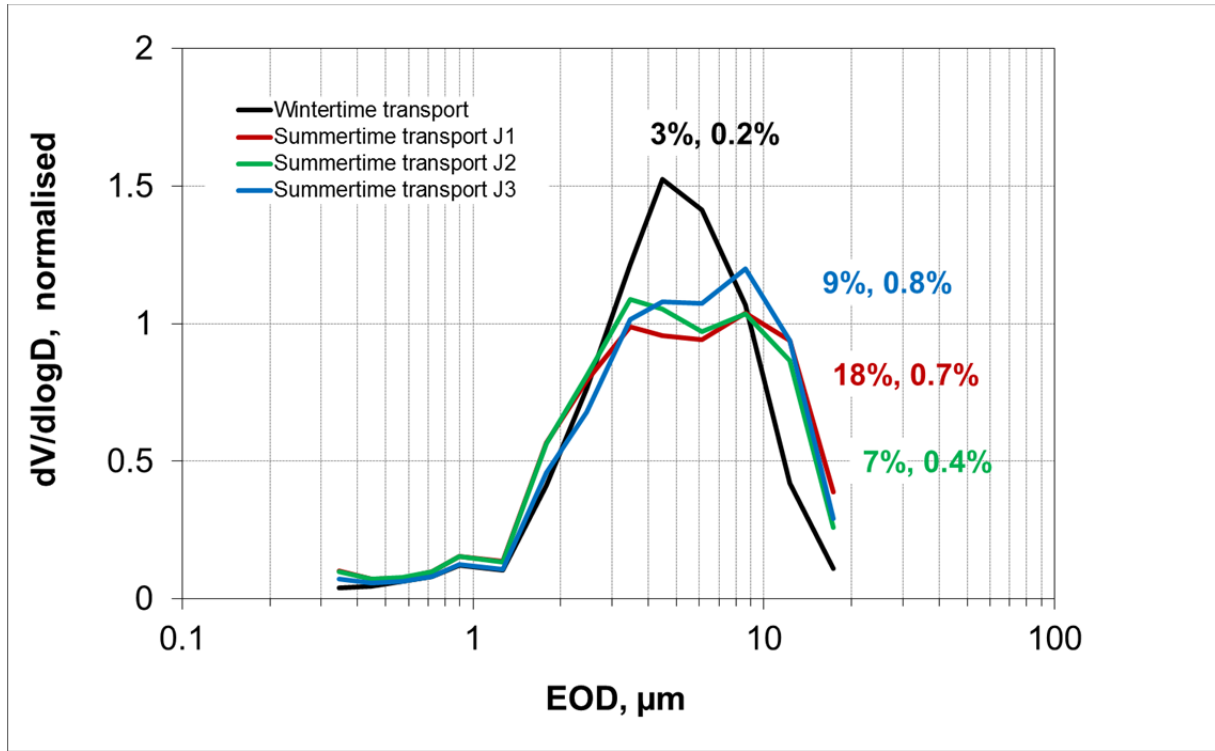
1596

1597 Figure 8. Scatterplot of the Ti/Fe ratio with respect to the Fe<sub>ox</sub>-to-Fe ratio. Open circles are  
1598 used to display values for samples corresponding to transport of Saharan dust, whereas  
1599 filled circles are for samples corresponding to local emission in the Sahel. Two grey points  
1600 indicates identified mixtures.



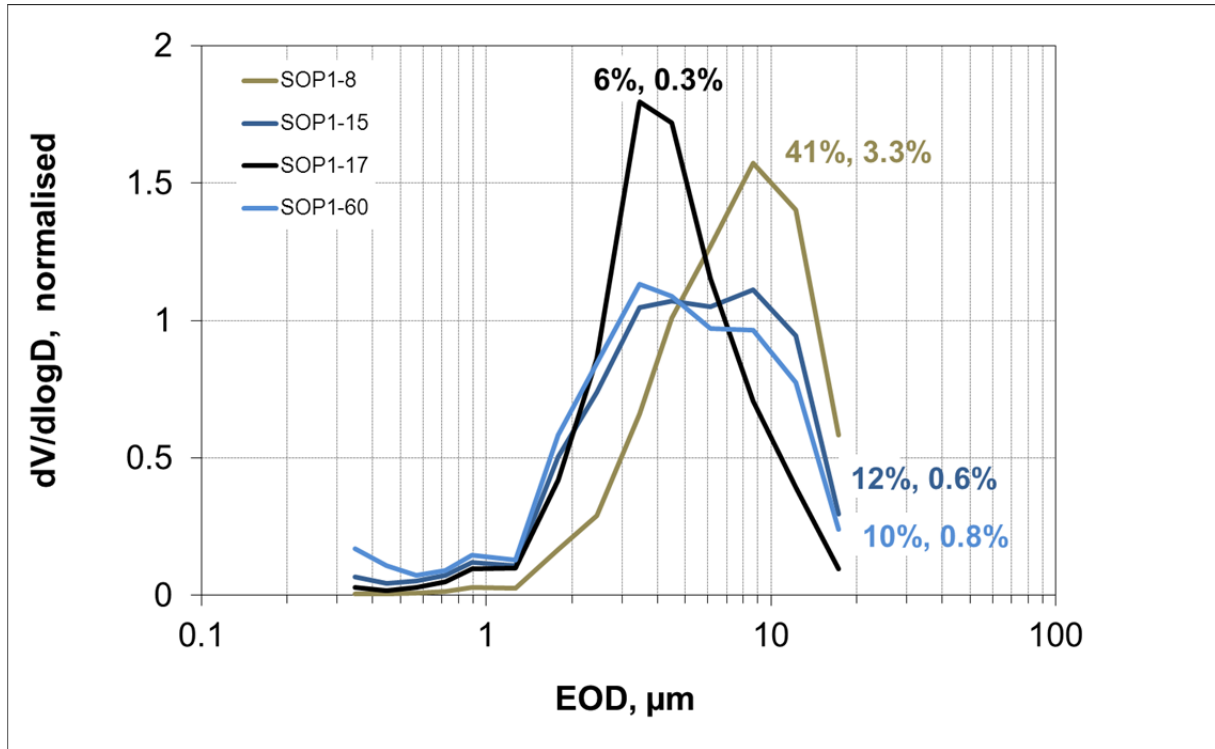
1601  
1602

1603 Figure 9. Normalized volume size distribution  $dV/d\log(EOD)$  at Banizoumbou during three  
 1604 consequent days in summer (J1 red line, J2 green line, J3 blue line) and one day in winter  
 1605 (black line) for samples representing dust transported from the Bodélé source region. Data  
 1606 are reported as a function of the equivalent optical diameter (EOD) as obtained by optical  
 1607 counter measurements without any corrections for the sample refractive index.



1608  
 1609  
 1610

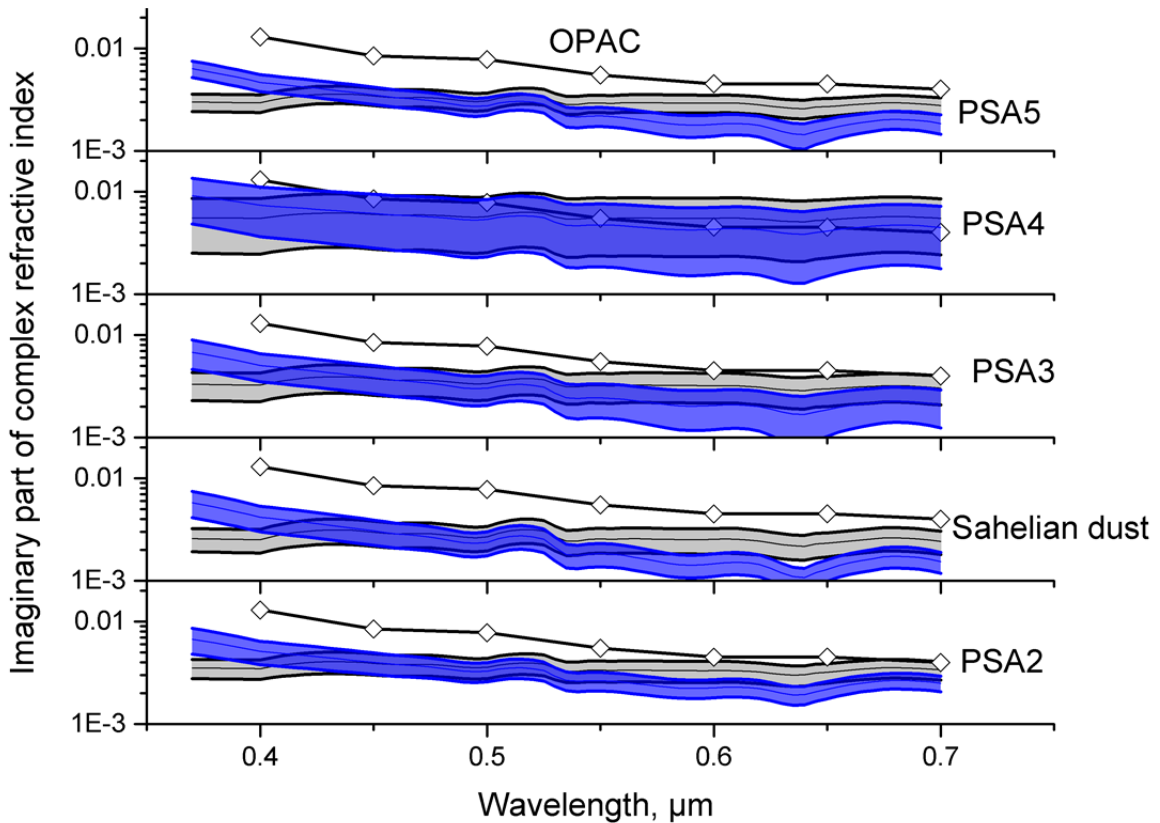
1611 Figure 10. Normalised volume size distribution  $dV/d\log(EOD)$  for samples representing  
 1612 Sahelian dust: SOP1-8 representing an episode of local emission by erosion; SOP1-15 and  
 1613 SOP1-60 representing the background dust composition in the absence of local erosion; and  
 1614 SOP1-17 representing the composition of Sahelian dust advected at the sampling site after  
 1615 having been emitted by local erosion in the proximity. Numbers represent the measured  
 1616 percent mass fraction of quartz and feldspars (sum of albite and ortoclase), respectively.



1617  
 1618



1619 Figure 11. Imaginary part of the complex refractive index calculated from the mineralogical  
 1620 composition of dust steaming from sources PSA5, PSA4, PSA3, local erosion in the Sahel,  
 1621 and PSA2 (from top to bottom). Figure 11.a represents the real part in the 0.3-0.7  $\mu\text{m}$ ,  
 1622 calculated assuming refractive index from Table 3. Grey shaded curves represent the mean  
 1623 values (light grey line) and 1 standard deviation (grey shaded areas) obtained when using  
 1624 the data from Bedidi and Cervelle (1993) for hematite, whereas blue shaded areas  
 1625 correspond to values calculated using the hematite data from Shettle (1979). The light blue  
 1626 line represents mean values and the blue shaded area represents one standard deviation.  
 1627 Figure 11.b represents the imaginary part of the complex refractive index calculated in the 6-  
 1628 16  $\mu\text{m}$  spectral domain. The black line with white diamonds represents data from the OPAC  
 1629 database (Hess et al., 1998).

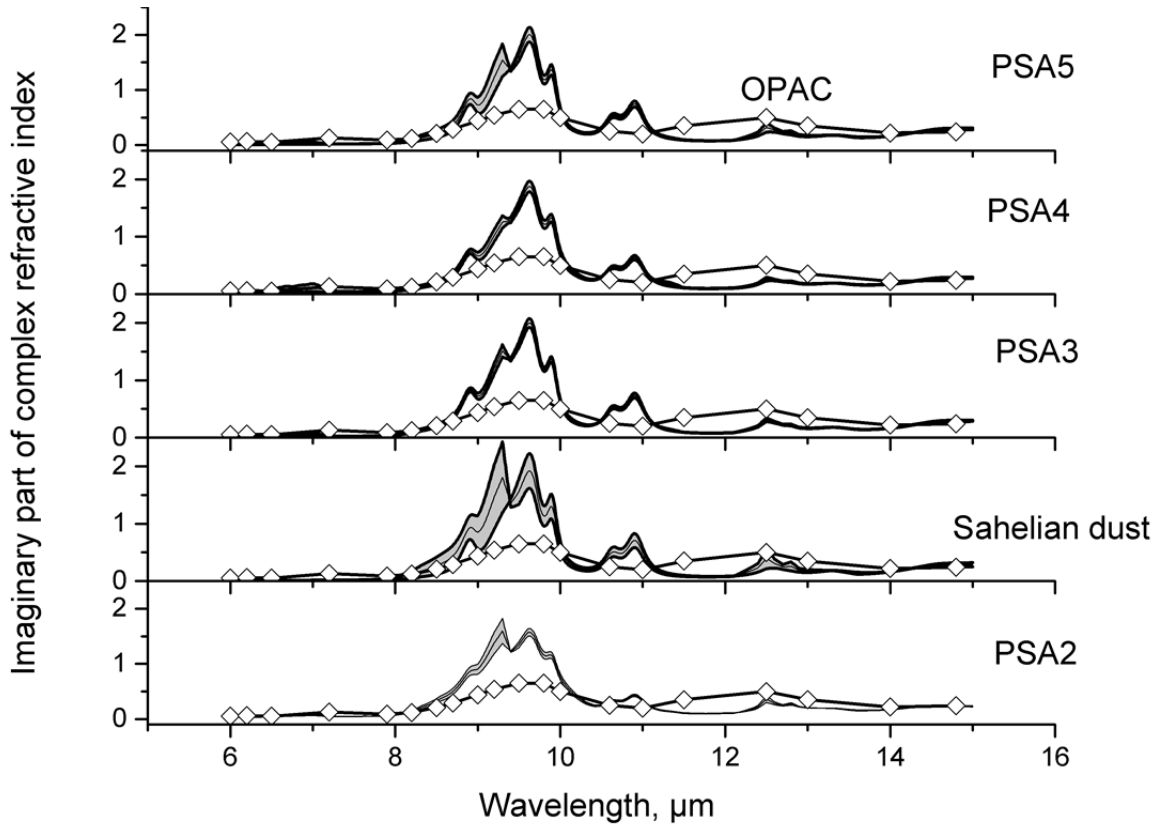


1630

1631

1632

1633 Figure 11. suite

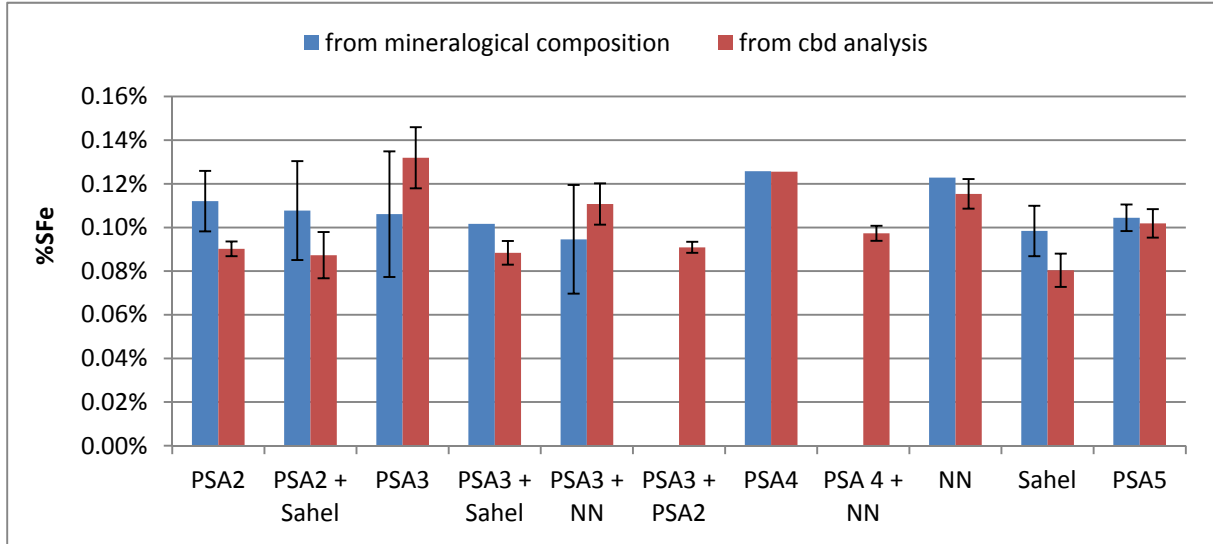


1634

1635

1636

1637 Figure 12. Iron solubility calculated from the mineralogical composition and from CBD  
1638 analysis as a function of emission source. Error bars indicate standard deviation. When error  
1639 bar is not presented, the data is only for one sample.



1640

1641